IIT RESEARCH INSTITUTE
Engineering Mechanics Division
Chicago, Illinois 60616

BASE FLOW AND SEPARATION STUDIES

by

R. S. Norman

FINAL REPORT

CONTRACT NO. NAS8-20392

September, 1968

NOV 1968
RECEIVED
NASA STI FACILITY
INPUT BRANCH

FACILITY FORM 602
N70-19762
(ACCESSION NUMBER)
102
(PAGES)
CR-102460
(NASA CR OR TMX OR AD NUMBER)
(THRU)
1
(CODE)
12
(CATEGORY)

Reproduced by the
CLEARINGHOUSE
for Federal Scientific & Technical
Information Springfield Va. 22151

This report was prepared by IIT Research Institute under Contract NAS8-20392, "Base Flow and Separation Studies," for the George C. Marshall Space Flight Center of the National Aeronautics and Space Administration. The work was administered under the technical direction of the Fluid Mechanics Research Office, Mr. I. P. Jones and Dr. F. R. Krause acting as project managers.

FOREWORD

This report describes the work performed by the IIT Research Institute for the National Aeronautics and Space Administration under Contract NAS8-20392. The work reported covers the period of research activity from June 22, 1966 to July 31, 1968.

The author wishes to acknowledge the technical direction and support of Dr. M. J. Fisher on this project. Also, Mr. J. A. Fitzgerald and Mr. S. J. Pernic contributed vitally to the experimental phases of the program. The excellent cooperation of Mr. S. T. Vick and his staff at the Rosemount Aero-Hypersonic Laboratory, where the wind tunnel tests were performed, was most appreciated.

Respectfully submitted,

IIT RESEARCH INSTITUTE

R. S. Norman
Research Engineer

APPROVED BY:

T. H. Schiffman
Assistant Director
Engineering Mechanics Division

/njn

ABSTRACT

This experimental study was performed at a Mach number of 2.97 over a Reynolds number range of 6.5×10^6 to 41×10^6. Measurements were made in the base recirculation region behind a two-dimensional, blunt trailing edge model. Base pressure values corresponded to previous experimental data. Hot wire measurements of mean and fluctuating velocities indicated turbulence intensities of 40 to 100 percent near the model base. Power spectra of the base boundary layer were similar to typical turbulent boundary layers. Total temperatures in the recirculation region were slightly less than free stream recovery temperature far from the base and showed a thin thermal boundary layer close to the cooled base surface. Heat transfer data showed that the base boundary layer was the major resistance to convective heating. Non-dimensionalized heat transfer coefficients showed little dependence on Reynolds number.

TABLE OF CONTENTS

	Page
SUMMARY	1
INTRODUCTION	2
SYMBOLS	4
APPARATUS AND TEST PROCEDURE	8
WIND TUNNEL	8
MODEL CONFIGURATION	8
INSTRUMENTATION	8
HOT WIRE ANEMOMETER TECHNIQUES	14
BASIC THEORY	14
END LOSS EVALUATION	16
WIRE CHARACTERISTICS	19
CALIBRATION PROCEDURE	20
RESULTS AND DISCUSSION	22
PRESSURE DATA	22
VELOCITY DATA	30
TOTAL TEMPERATURE DATA	35
HEAT TRANSFER DATA	36
SCALING EFFECTS	43
CONCLUSIONS	45
RECOMMENDATIONS	48
REFERENCES	50
FIGURES	52

LIST OF ILLUSTRATIONS

Figure

1 Wind Tunnel Model Cross Sectional Dimensions

2 Model Installation on Removable Wind Tunnel Wall Section

3 Probing Base Plate Configuration

4 Low Density Calibration Apparatus

5 Transducer Base Plate and Shoulder Section

6 Schematic of Transducer Installation

7 View of Transducer Base Plate Installed in Model with Cover Plate Removed

8 Heat Transfer Base Plate

9 Linearizer Output Voltage Versus Mean Air Flow Velocity at Atmospheric Pressure

10 Hot Wire Current Versus Temperature Difference

11 Bridge Voltage and Linearizer Voltage Versus Mean Air Flow Velocity

12 Calibration of Hot Wire Probe TS4 at Four Pressure Levels

13 Shoulder to Total Pressure Ratio Versus Reynolds Number

14 Base to Shoulder Pressure Ratio Versus Reynolds Number at $M_\infty = 2.97$

15 Qualitative Shape of p_b/p_s Curve as Reynolds Number Varies. Hama Reference

16 Comparison of Measured Base Pressure Ratio Versus Mach Number with Previous Results

17 Location of Static Taps on Wind Tunnel Wall

18 Tunnel Wall to Model Shoulder Pressure Ratio Versus Distance from Base

LIST OF ILLUSTRATIONS (Cont'd)

Figure

19 Shadowgraphs of Base Recirculation Region at $M_\infty = 2.97$ and Three Reynolds Numbers

20 RMS Pressure Levels from Miniature and Large PZT-5H Transducers

21 Power Spectral Density for PZT Gauge #3 Located Near Base Center

22 RMS Pressure Levels for Large Gauges at Unchoked Control Valve Conditions

23 Power Spectral Density for Large Transducer Gauge No. 6 on Base Plate

24 Cross-Correlation of Several Pressure Transducers for Choked Control Valve

25 Cross-Correlation Coefficient for Pressure Transducer Gauges 11 and 12; 11 and 6

26 Non-normalized Power Spectra for Base Gauges 2 and 4

27 Non-normalized Power Spectra for Equal Signals from Gauges 2 and 4

28 Cross-Correlation for Pressure Transducer Gauges 2 and 4 over 1/3 Octave at 10,000 Hz

29 Base Boundary Layer Profile for Several Reynolds Numbers

30 Base Boundary Layer Profile for Three Probe Positions

31 RMS Velocity Versus Distance from Base at High Reynolds Numbers

32 Turbulence Intensity $U_{RMS}/\overline{U}$ Versus Distance from Base for Probe Position (2P)

33 Power Spectral Density for Hot Wire Probe H1 for Several Reynolds Numbers

34 Power Spectral Density for Hot Wire Probe H2 for Various Distances from Base

LIST OF ILLUSTRATIONS (Cont'd)

Figure

35 Cross-Correlation of Hot Wires H1 and H2 Including Computation of Convection Velocity

36 Recirculation Temperature to Total Temperature Ratio Versus Distance from Base for TC3

37 Recirculation Temperature Ratio Versus Base Temperature Ratio for Three Thermocouple Probes and Several Reynolds Numbers

38 Recirculation Temperature Ratio Versus Base Temperature Ratio for Different x Distances

39 Computation of Heat Transfer Coefficient from Transient Base Plate Temperature Rise

40 Distribution of Total Heat Transfer Coefficient Over Base Plate for $Re_\infty = 39.2 \times 10^6$

41 Schematic of Base Flow Recirculation Region

42 Distribution of Total Heat Transfer Coefficient Over Base Plate for $Re_\infty = 6.8 \times 10^6$

43 Average Heat Transfer Coefficient Versus Reynolds Number

44 Total Stanton Number Versus Reynolds Number for Different Base Temperatures

45 Shear Layer Stanton Number Versus Reynolds Number for Different Base Temperatures

46 Base Pressure Ratio Comparison for Two-Dimensional and Axisymmetric Theories

47 Base Pressure Ratio Versus Mach Number for Saturn S-IC Booster Model

SUMMARY

An experimental investigation was performed at a free stream Mach number of 2.97 over a free stream Reynolds number range of 6.5×10^6 to 41×10^6 to determine the separated base flow characteristics of a pointed ogive, two-dimensional, blunt trailing edge model. Static pressures, mean and fluctuating velocities, total temperature, and heat transfer measurements were made in the recirculating flow region behind the model base. Velocity measurements were made with traversing hot wire anemometer probes. Heat transfer measurements utilized a transient technique with the model cooled below ambient temperature with liquid nitrogen. Fluctuating pressure measurements were not successful because of transducer sensitivity to model vibration.

Base pressures were compared with previous theory and data and showed good agreement with past data for thin approach shoulder boundary layers. Mean and fluctuating velocity measurements indicated high levels of turbulence intensity as the base was approached from the rear. Turbulence intensities of 40 to 100 percent were found. The mean velocity measurements defined a base boundary layer which exhibited power spectral densities similar to typical turbulent boundary layers.

For sections of the recirculation region far from the base, the total temperature was slightly less than free stream recovery temperature and not affected by Reynolds number. Close to the base a thermal boundary layer was measured which was influenced by base temperature and Reynolds number. Heat transfer data showed that the base boundary layer provided the major resistance (87 percent) to convective base heating. Nondimensionalized heat transfer coefficients showed little dependence on Reynolds number.

INTRODUCTION

The base heating problem related to multi-engine rocket boosters has been under investigation since the 1950's. Three sources of heat transfer have been found for the complex interactions between engine plumes and free stream air flow. The impingement of two or more engine exhaust plumes can cause recirculation of hot gases toward the vehicle base. This is a convective flow situation and can cause high heating rates at altitude as well as at sea level take-off conditions. The second source of heat transfer is thermal radiation from the luminous gas plumes. The radiation heat transfer is a function of the plume temperature and emissivity as well as the form factor between the volume of luminous gases and the base. Finally, the recirculation of fuel-rich turbine exhaust gases into the base region can produce a combustible mix which will ignite under certain conditions. This erratic phenomenon is called base burning and can produce locally high heat transfer rates.

This research project investigates the flow recirculation characteristics which are important for convective heat transfer. In order to simulate the base heating of a large, multi-engine, rocket booster, past experiments have been performed with complex models of the booster. These models have sometimes had small rocket engines to simulate the correct plume temperature and impingement configuration. Test results have been applicable to the particular geometry of the model. The present work is directed toward a simple separated base flow configuration which can be applied more generally.

The model tested here was a two-dimensional, pointed-ogive, blunt trailing edge body. The wind tunnel used unheated air at a Mach number of 2.97 and a Reynolds number range of 6.5×10^6 to 41×10^6. This model has been previously tested

at lower Reynolds numbers [Ref. 1], and current experiments were designed to extend past results to higher Reynolds numbers and provide some additional measurement capability. Static and fluctuating pressures, mean and fluctuating velocities, total temperature, and heat transferred to the base were measured in the separated base flow region. Primary emphasis was placed on the turbulence characteristics of the recirculation region and the effect these characteristics have on the basic flow relationships.

SYMBOLS

A	Cross sectional area
A', A''	Constants for hot wire equations
a	Local speed of sound
B', B''	Constants for hot wire equations
C	Crocco number $C = 1 + \left(\frac{2}{(\gamma-1)M^2}\right)^{-1/2}$
C', C'', C'''	Constants in hot wire linearizer equation
C_p	Specific heat
D	Transducer gauge diameter
d	Hot wire diameter
E	Total hot wire bridge voltage, $\overline{E} + e'$
$\overline{E}$	Mean hot wire bridge voltage
$\overline{E}_{lin}$	Mean hot wire linearizer voltage
e'	Fluctuating hot wire bridge voltage
e_{RMS}	RMS value of fluctuating voltage, $\overline{(e'^2)}^{1/2}$
$e_{RMS\ 1/3}$	RMS value of fluctuating voltage in a 1/3-octave bandwidth
f	Frequency
Δf	1/3 octave bandwidth
g	Thickness
h	Convective heat transfer coefficient
I	Hot wire current
k	Thermal conductivity
K', K''	Coefficients in hot wire heat balance equation

$K(R)$	Function of bridge resistances which is constant for a given hot wire resistance
L	Model length
ℓ	Hot wire length
M	Mach number, $\overline{U}/a$
m	Slope of $\overline{E}$ versus $\overline{U}$ calibration curve
Nu_d	Nusselt number based on hot wire diameter, hd/k
P	Stagnation pressure
PZT	Lead-zirconate-titanate
p	Static pressure
p_{RMS}	RMS value of fluctuating pressure
q	Dynamic pressure, $(\gamma/2)pM^2$
$\dot{Q}$	Total heating rate
R	Hot wire resistance
Re_d	Reynolds number based on hot wire diameter, $\overline{U}d\rho/\mu$
Re_∞	Reynolds number based on free stream conditions and model length, $\overline{U}_\infty L\rho_\infty/\mu_\infty$
$r(\xi,\tau)$	Space-time correlation coefficient between two hot wires or one wire and one transducer
$r(\eta,\tau)$	Space-time correlation coefficient between pressure transducers
S_a, S_b	Total transducer signals
St	Stanton number, $h/\rho\overline{U}C_p$
T	Temperature
t	Time
U	Total velocity, $\overline{U} + U'$
$\overline{U}$	Mean total velocity
U'	Fluctuating component of total velocity

U_{RMS}	RMS value of fluctuating velocity, $\overline{(U'^2)}^{1/2}$
V	Manipulated pressure transducer signals
X, X_a, X_b	Correlated vibration signals from pressure transducers
x	Coordinate axis; Distance from base (Fig. 5); Also distance along hot wire
Y, Y_a, Y_b	Uncorrelated pressure signals from pressure transducers
y,z	Coordinate axes (Fig. 8)
α	Temperature coefficient of resistance
γ	Specific heat ratio
θ	Temperature difference, $T_{hw}-T_e$
μ	Dynamic viscosity
ρ	Density of air, or hot wire electrical resistivity
σ	Spreading factor, $12.0 + 2.76\ M_2$
σ_{sb}	Stefan-Boltzmann constant
τ	Time delay
ω	Specific weight
ξ	Separation distance for correlation measurements between two hot wires or one wire and one transducer
η	Separation distance for correlation measurements between pressure transducers

Subscripts

B	Recirculation zone
Br	Effective recirculation zone recovery value
BP	Refers to heat transfer coefficient across base plate boundary layer
b	Base plate

c	Convected value of velocity
e	Ambient air value
hw	Hot wire
hwm	Mean hot wire
o	Reference value
p	Pressure signal only
r	Wind tunnel recovery value
SL	Refers to heat transfer coefficient across free shear layer
s	Model shoulder value just ahead of base corner
TOT	Refers to total heat transfer coefficient across recirculation region
t	Tunnel stagnation
v	Vibration signal only
w	Tunnel wall static
2	Outer edge of free shear layer
∞	Free stream static

APPARATUS AND TEST PROCEDURE

WIND TUNNEL

The present investigation was conducted in the University of Minnesota Aero-Hypersonic Laboratory at Rosemount, Minnesota [2]. The experiments were made in the 6 x 9 in. (15.24 x 22.86 cm) Supersonic Blowdown Wind Tunnel at a Mach number of 2.97. The maximum air stagnation pressure was 345 psia (238 N/cm^2) while stagnation temperature was approximately ambient air temperature. The unit Reynolds number varied from 10^7 to 6×10^7 1/ft (3.3×10^7 to 19.7×10^7 1/m) with corresponding run time variation between 20 and 8 seconds.

MODEL CONFIGURATION

The model was a two-dimensional tangent ogive design. Figure 1 shows the model cross-section dimensions. This model had been previously used primarily in the Aero-Hypersonic Laboratory 6 x 9 in. (15.24 x 22.86 cm) Continuous Wind Tunnel [1]. Installation in the wind tunnel was accomplished by side mounting the model on a removable tunnel wall section (Fig. 2). The model had an 8.0 in. (20.3 cm) chord and completely spanned the tunnel to reduce end effects. Provision was made for internal cooling of a cavity in the base plate assembly using liquid nitrogen.

INSTRUMENTATION

Since the base flow recirculation region was of primary interest in this study, three different base plates were used. The variables which were measured on the base plate itself were static and fluctuating pressures, mean temperature and heat transfer rate. Hot wire anemometer and thermocouple probes were traversed axially into the recirculation region to measure mean and fluctuating velocities and total temperatures, respectively.

Probing Base Plate

Figure 3(a) shows the geometrical layout of the probing base plate. This base plate was used for previous tests at lower densities [1]. Each base plate was inserted into the back of the hollow forebody. Instrumentation was routed through the forebody and out the side mounting plate. The three probing holes were used to traverse special Thermo-Systems, Inc. hot wire probes. The sensing element was a 0.00015 in. (0.00038 cm) diameter by 0.050 in. (0.127 cm) long tungsten wire supported by a flexible 0.062 in. (0.1575 cm) O.D. shaft. A sketch of the probe geometry is shown on Fig. 3(b). The shaft acted as the outer casing for the small coaxial conductors which connected the hot wire to the low-resistance lead-in cable. The plug-in end of the shaft was inserted into a probing hole from the rear of the model. The shaft then bent through 90° inside a 0.125 in. (0.318 cm) O.D. stainless steel tube and passed through the wall mounting plate. The tube was sealed to atmospheric pressure and the shaft locked to a micrometer adjustment screw which was used to position the hot wire as close as 0.010 in. (0.025 cm) from the base plate. An accurate reference position was obtained using a traversing telescope.

The mean output bridge voltage of the hot wire probe was read on a Thermo-Systems, Inc. Model 1010A Constant Temperature Anemometer without linearizer. The fluctuating component of the bridge voltage was recorded on an Ampex FR-1300 tape recorder. A 1/3 octave analyzer (Brüel and Kjaer audio frequency spectrometer Type 2112) was used to obtain power spectra for the fluctuating bridge voltage.

Each hot wire probe was calibrated in a small low-density flow rig. A schematic drawing of this rig is shown in Fig. 4. The system was evacuated to a specific pressure using valve A. A "leak" was introduced into the system through valve B. By adjusting valves A and B, the velocity through the

"test section" could be varied while the operating pressure level remained essentially constant. A set of manometers was used to record total pressure level and the difference between total and static pressure in the "test section." The calibration range attained was 30 to 200 ft/sec (9.2 to 61 M/sec) in velocity for total pressures varying from 1/60 to 1/10 atm.

The probing holes were also used to traverse 3 thermocouple probes. These were similar in geometry to the hot wire probes, except that the sensing element was an iron-constantan thermocouple junction, Fig. 3(c). These thermocouple probes were used to survey the temperature field in the recirculation region. When the model base was cooled to different below ambient temperatures, the thermocouples were traversed from very close to the base plate into the separated base flow region. Measurements were also taken for base temperatures equal to room temperature. Continuous recording of thermocouple probe outputs was made with Honeywell Brown chart recorders.

Several static pressure taps were located on the probing base plate to evaluate possible vertical or horizontal pressure gradients. These taps were connected to a mercury manometer board which could be clamped off after steady state pressures had been achieved. The board was photographed after a blowdown run and readings taken from the photograph.

The base plate was fabricated as a sealed box structure so that liquid nitrogen could be recirculated within the hollow box. Copper-constantan thermocouples were soldered to the inner side of the base plate surface [0.062 in. (0.1575 cm) thick 302 stainless steel] to record temperatures during cooled model runs.

Transducer Base Plate

A second base plate was built primarily for fluctuating pressure measurements. Miniature lead-zirconate-titanate piezoelectric discs were mounted in a vertical slot in this base plate (Fig. 5). These transducers were used previously at IITRI [3] and were selected for their very small dimensions. To survey the turbulence characteristics of the base half-height, several transducers had to be mounted in a distance of 0.75 in. (1.9 cm). This dictated using a transducer disc with nominal diameter of 0.025 in. (0.0635 cm) and 0.010 in. (0.025 cm) thick (Fig. 6). Two discs were cemented together with the faces of like polarity in contact to reduce the impedance of the transducer combination without affecting the pressure sensitivity. Connection from the transducer gauge to a Microdot connector was made with 0.001 in. (0.0025 cm) copper-nickel wire encased in a Teflon® sleeve. Figure 7 shows the Microdot connectors installed in the model. The slot cut in the base plate was filled with resilient RTV-118 so that a thin layer covered the top of each gauge and formed a flush surface. One larger gauge [0.062 in. (0.1575 cm) diameter by 0.040 in. (0.102 cm) thick] was mounted as shown in Fig. 5 for comparison with the miniature gauges. Also, the gauge mounted just below the model centerline was recessed below the surface and covered with epoxy so that it would not respond to pressure fluctuations. The output of this gauge would then be a measure of acceleration and/or model temperature variation effects. Further efforts were made to reduce vibration by making this base plate from solid brass, 13/16 in. (2.08 cm) thick. The base surface was then flash chrome plated to provide a hard finish. Because of the temperature sensitivity of these transducers, this base plate was only tested at ambient temperatures.

The transducers were checked out by subjecting the base plate to calibrated pressure pulses. The section of the base

plate face containing the transducers was sealed off so that pressurized air could be released by a fast acting solenoid valve to produce a pressure step on the gauges. An oscilloscope trace was made of each transducer response and values of voltage output versus pressure step level were recorded.

The transducer output was recorded on an Ampex FR-1300 tape recorder. Power spectra and correlation measurements were performed using the B&K spectrometer and a Honeywell 9410 correlator, respectively.

Static pressure taps were included as a reference. Also, copper-constantan thermocouples were imbedded in the brass base plate close to the surface to record possible base temperature changes during a run. In addition, probing holes H1 and H2 were located in this base plate to make correlation measurements between two hot wire probes.

Heat Transfer Base Plate

To evaluate the heat transferred through the jet shear layer and separated base flow region to the base, a special heat transfer base plate was constructed. This base plate was formed from a block of linen bakelite. A cavity was machined in one side of the block so that liquid nitrogen could be used to cool the whole assembly. The bakelite acted as thermal insulation for a thin sheet of pure nickel [0.025 in. (0.0635 cm) thick] which was epoxyed to the bakelite block (Fig. 8). A special Hysol Corporation epoxy (R8-2038 resin and H8L-3460 hardener) was found to be a good bonding agent for nickel and bakelite from room temperature down to 160°R (89°K). During the transient heating period, the increase in thermal capacity of 15 nickel discs was measured with a copper-constantan thermocouple junction located on the back of each disc. Lateral heat conduction was minimized by epoxying the discs, which were the same thickness

as the nickel plate, to the bakelite. The thermocouple wires used were 0.010 in. (0.025 cm) diameter to minimize heat conduction losses along their lengths. The thermocouple millivolt output was recorded by a Brown chart recorder as a function of time.

Shoulder Approach Flow

The model shoulder ahead of the base was instrumented to record static and fluctuating pressures. The static pressures were used to compute tunnel Mach numbers since there was no permanent test section instrumentation. Four miniature and two large PZT-5H transducers were mounted on a special model section to investigate the turbulence characteristics of the shoulder approach flow (Fig. 5).

Auxiliary Measurements

Shadowgraph photos were taken of the complete near wake flow at all Reynolds numbers tested. For certain runs the 5 in. (12.7 cm) diameter window on the tunnel wall was replaced with an aluminum blank which had an array of static taps to measure pressures throughout the separated flow region. Originally, these static pressures were to be measured with a vertical splitter plate surrounding the midspan section of the model. However, the first splitter plate failed during a checkout run due to inadequate structural support. It was decided that further attempts to measure static pressures in the wake would be done on the tunnel side wall.

A chart record was made of the tunnel stagnation temperature variation during a run. Since the tunnel air supply was stored outside and was not heated, the stagnation temperature dropped slightly during a run. The stagnation pressure was set using a Heise gauge and controlled manually. A Kistler model (601A) transducer was mounted in the tunnel stagnation region to measure the wind tunnel background noise.

HOT WIRE ANEMOMETER TECHNIQUES

BASIC THEORY

Previous tests with this model had been carried out at the low base density of about 1/100 of an atmosphere [1]. The accuracy of constant temperature hot wire anemometers suffers greatly at low densities because the principle of operation depends on the mass flow over the hot wire. At a given density as the air velocity over the wire increases, the increased heat transfer rate tends to cool the wire. To maintain a constant wire temperature, the anemometer circuitry must increase the bridge voltage. At atmospheric density and for reasonable flow velocities, the relationship between anemometer bridge voltage and air flow velocity is:

$$\overline{E}^2 K(R) = [A' + B' \overline{U}^{1/2}](T_{hw} - T_e) \qquad (1)$$

where $\overline{E}$ = mean bridge voltage
$K(R)$ = a function of bridge resistances which is constant for a given hot wire resistance (i.e., temperature)
T_{hw} = hot wire temperature
T_e = air flow temperature
$\overline{U}$ = air flow mean velocity
A', B' = constants depending on wire geometry.

This relationship for air flow over a heated cylinder was first proposed by King in 1914 [4]. We can relate the wire resistance to its temperature through the equation:

$$R_{hw} = R_o [1 + \alpha(T_{hw} - T_o)] \qquad (2)$$

where R_{hw} = wire resistance at elevated temperature T_{hw}
R_o = wire resistance at some reference temperature T_o
α = temperature coefficient of resistance for the wire material

The reference resistance can be computed from the formula

$$R_o = \rho_o \frac{\ell}{A_{hw}}$$

where ρ_o, ℓ, and A_{hw} are the wire electrical resistivity, length, and cross-sectional area respectively. Therefore, by knowing the wire material properties, setting operation at a particular wire temperature T_{hw}, and assuming constant T_e, Eq. (1) becomes

$$\overline{E}^2 = A'' + B'' \overline{U}^{1/2} \tag{3}$$

It is desirable to have a linear relationship between velocity and voltage for turbulence computations. This is done through manipulations on the bridge voltage output, $\overline{E}$. The particular linearizer used here modified $\overline{E}$ with squaring circuits. Solving Eq. (3) for $\overline{U}$,

$$\overline{U} = \frac{1}{B''^2} (\overline{E}^2 - A'')^2$$

The linearizer first squares $\overline{E}$, then subtracts A", and finally squares the difference. The resulting value is called the linearizer voltage, $\overline{E}_{lin}$. Thus,

$$\overline{E}_{lin} = (\overline{E}^2 - A'')^2$$

Figure 9 is an example of the output from the linearizer as a function of flow velocity. This calibration was accomplished by mounting one of the special hot wire probes in the potential core of a one inch (2.54 cm) diameter subsonic, converging nozzle exhausting into the atmosphere. The hot wire then measures the mean flow velocity since the turbulence level in the potential core is negligible. For velocities over 100 ft/sec (30.5 m/sec), the plot is essentially linear. However, as the velocity approaches zero a definite curvature is noticeable. Therefore, for this experiment the relationships of

Eq. (1) do not hold at velocities below 100 ft/sec (30.5 m/sec). King [4] actually presented two formulas for the heat loss from a cylinder due to convection. The first expression for large velocities leads to Eq. (1). The second gives

$$\overline{E}^2 = C' \left(\frac{1}{C'' + C''' \log \frac{1}{\overline{U}}} \right) \tag{4}$$

for small velocities. The difficulty develops in evaluating the constants in Eq. (4). The material properties of the wire, mounting procedures, and wire geometry must all be considered. Also, as the velocity decreases the heat conducted away from the hot wire through the supports becomes more significant. King's original experiments were conducted with very long platinum wires so that the end losses could be neglected. In order to make miniature probes, present day hot wires have much lower values of ℓ/d (sensing length/wire diameter) than King's geometry. For example, an average ℓ/d for the King experiments was 6000. The tungsten wires used for IITRI experiments had an ℓ/d of about 300. The ratio has dropped by a factor of 20.

END LOSS EVALUATION

Davies and Fisher presented an analysis of the end losses from an electrically heated cylindrical wire in 1964 [5]. The wire temperature was assumed to vary along its length. A simple heat balance on the wire was stated:

> Heat generated in the wire per unit length by an electric current I = heat loss through conduction to supports + heat loss by convection, per unit length + heat loss by radiation, per unit length.

By assuming that the wire conductivity k_{hw} was constant over the temperature interval considered, the governing differential equation was shown to be

$$\frac{I^2\rho_{hw}}{A_{hw}} + k_{hw}A_{hw}\frac{d^2T_{hw}}{dx^2} - \pi d\,[h_{hw}(T_{hw} - T_e) + \sigma_{sb}(T_{hw}^4 - T_e^4)] = 0 \tag{5}$$

where T_{hw} = wire temperature varying along the length
T_e = ambient surrounding temperature
$\rho_{hw} = \rho_o[1 + \alpha(T_{hw} - T_o)]$, electrical resistivity
T_o = reference temperature
h_{hw} = convective heat transfer coefficient, assumed constant
σ_{sb} = Stefan-Boltzmann constant
A_{hw} = wire cross-sectional area, $\pi d^2/4$

Assuming that the radiation constant is small, $T_o = T_e$, and setting $\theta = T_{hw} - T_e$, Eq. (5) becomes

$$\frac{I^2\rho_o(1+\alpha\theta)}{A_{hw}} + k_{hw}A_{hw}\frac{d^2\theta}{dx^2} - \pi d h_{hw}\theta = 0$$

or

$$\frac{d^2\theta}{dx^2} + \left[\frac{I^2\rho_o\alpha}{k_{hw}A_{hw}^2} - \frac{\pi d h_{hw}}{k_{hw}A_{hw}}\right]\theta + \frac{I^2\rho_o}{k_{hw}A_{hw}^2} = 0$$

$$\frac{d^2\theta}{dx^2} + K'\theta + K'' = 0 \tag{6}$$

$$K' = \frac{I^2\rho_o\alpha}{k_{hw}A_{hw}^2} - \frac{\pi d h_{hw}}{k_{hw}A_{hw}}$$

$$K'' = \frac{I^2\rho_o}{k_{hw}A_{hw}^2}$$

Now let the origin of the x coordinate system be at the center of the wire which has a length ℓ. The boundary conditions become,

at $x = 0$, $\frac{d\theta}{dx} = 0$, for airflow normal to the wire

at $x = \pm\,\ell/2$, $\theta = 0$, $T_{hw} = T_o$

Davies and Fisher show that for K' negative (h_{hw} relatively large) the solution to Eq. (6) is

$$\theta = \frac{K''}{K'}\left[\frac{\cosh\sqrt{|K'|}\ x}{\cosh\sqrt{|K'|}\ \ell/2} - 1\right]$$

where $|K'|$ is the absolute value of K'. Integration along the length of the wire gives the mean wire temperature, T_{hwm}

$$T_{hwm} = T_o + \frac{K''}{K'}\left[\frac{\tanh\sqrt{|K'|}\ \ell/2}{\sqrt{|K'|}\ \ell/2} - 1\right] \tag{7}$$

For K' positive, particularly when $h_{hw} = 0$, the solution to Eq. (6) takes a different form,

$$T_{hwm} = T_o + \frac{K''}{K'}\left[\frac{\tan\sqrt{K'}\ \ell/2}{\sqrt{K'}\ \ell/2} - 1\right] \tag{8}$$

Equations (7) and (8) can be used for a parametric study involving T_{hwm}, h_{hw}, and I, the three unknowns. By specifying a particular wire material, geometry, and discrete values of h_{hw}, a plot of wire current versus $T_{hwm}-T_o$ can be developed. Figure 10 shows such a plot for the particular tungsten wires used. In these experiments the value of $(T_{hwm}-T_o)$ used was 202°R (112°K). The maximum value of h_{hw} can be roughly calculated from the relationship for air flowing over a heated cylinder [6].

$$Nu_d = 0.43 + 0.48\ (Re_d)^{0.5} \tag{9}$$

for Re_d between 1 and 4000.

For the base separated flow region, the maximum density and velocity conditions gave a Reynolds number based on wire diameter of nearly one. Then, for $Nu_d = 0.91$, $h_{hw} \simeq 1240$ BTU/hr ft^2 °R (0.7 watts/cm^2 °K). The vertical line on Fig. 10 shows the theoretical wire currents for this particular test.

It is apparent that the end loss quantity (which is a function of I^2 at $h_{hw} = 0$) is significant over much of the test range. For the lowest base pressures and recirculation velocities measured, $Re_d \ll 1$ and Eq. (9) is not valid. Under these conditions, intuitively, h_{hw} approaches zero, and the end loss is a major part of the total heat loss.

WIRE CHARACTERISTICS

The hot wire mounting system was dictated by the base geometry and the long, thin support rod. A hot wire system was chosen over a hot film because of the much smaller diameter wires available. The smallest film sensor (e.g., a platinum coated glass rod) available is 0.001 in. (0.0025 cm) whereas tungsten wires are available with 0.00015 in. (0.00038 cm) diameter. Therefore, the hot wire is better suited to conditions of very small turbulence scales and large velocity gradients. Also, the bare wire has a much better frequency response than the thin film which is necessary to evaluate high frequency turbulence levels. Tungsten was chosen as the wire material because of its high temperature coefficient of resistance [α = 0.0045/°K (0.0025/°R)] and high strength. Strength was an important consideration because of the high impulse loading on the model during the wind tunnel starting sequence and the dust particles in the tunnel flow.

Unfortunately, the oxidation properties of tungsten restricted the operating temperature of the wire. It is important that the wire reference resistance (R_o) remains nearly constant while the wire is being used. The wire "overheat" ratio R_{hw}/R_o defines the operating temperature through

$$\frac{R_{hw}}{R_o} = 1 + \alpha \, (T_{hw} - T_o) \tag{10}$$

A fixed calibrated resistor was used in the anemometer for R_{hw}. When R_o increases due to oxidation effects, the overheat ratio decreases and therefore T_{hw} also decreases. This changes the initial calibration of the wire. Some sources say that tungsten may be operated up to 1120°R (623°K) without severe oxidation. However, a check with one wire at 1030°R (573°K) showed a sharp drop in bridge voltage in a few minutes indicating rapid oxidation. This wire was then unusable. After other tests, an overheat value of approximately 1.5 was found to produce fairly stable results. This resulted in a rather low wire temperature of 720°R (400°K). The bridge voltage level was then lower than optimum, and therefore the change in voltage with a change in velocity was smaller than desirable.

CALIBRATION PROCEDURE

All of the hot wires used were calibrated in the low-density flow rig shown in Fig. 4. Figure 11 shows typical calibration curves for four wires at a pressure level of 0.10 atmospheres. The wires are all set with the same fixed operating resistance of 12.0 ohms. The wide variation in the curves of $\overline{E}$ versus velocity shows that although all wires have the same nominal length and diameter, the geometry differences from the average, the individual solder joints, and the different wire surface conditions all contribute to give each wire a particular calibration curve. Significantly, the linearizer output $\overline{E}_{lin}$ is not linear over the velocity range tested. As demonstrated earlier (Fig. 9), at low mass flows the linearizer squaring circuitry is not applicable. If a linearizer were available with an arbitrary shaping function, a linear output could be obtained in this range. IITRI has such a linearizer, but it was not compatible with the hot wire anemometer and model constraints. Therefore, it was decided to use the hot wires without linearizing and to calibrate each wire at the density

levels expected during the tests. Figure 12 shows a typical calibration curve for one wire. To evaluate a fluctuating velocity component, the slope of the $\overline{E}$ vs. $\overline{U}$ curve is required at the particular mean velocity value.

RESULTS AND DISCUSSION

The presentation of results begins with the pressure data. Static pressures, RMS fluctuating pressure levels, and spectra, are discussed. Similar quantities are then presented for velocities in the base region. Finally, the heat transfer results are shown and compared with previous data and theory.

PRESSURE DATA

Static Pressure Measurements

Model shoulder static taps just ahead of the base were used to determine the free stream Mach number. Additional streamwise taps were used to assure that the flow had fully recovered from the leading edge shock wave. Figure 13 shows the ratio of shoulder to stagnation pressure ratio versus Reynolds number based on model chord length. A free stream Mach number of 2.97 was determined from these measurements.

The vertical array of static taps on the probing base plate (Fig. 3) did not show any consistent trend for a given run. Therefore, an average base pressure was computed from several of the static taps on the base. Figure 14 plots base to shoulder pressure ratio versus Reynolds number for the present data and for Ref. [1]. The present results appear to follow the same trend as the untripped boundary layer data of Ref. [1] but are displaced slightly to the right. This is not unexpected since the current model tests were made with no tripping device because most of the runs were at the high Reynolds numbers. The shift is attributed mainly to the fact that two different wind tunnels were used. Each tunnel would have its own free stream turbulence characteristics and transition range. Also, the forebody shape may have been altered slightly during resurfacing of the model. The Ref. [1] tripped boundary layer data show approximately the same minimum p_b/p_s

as was found at the highest Reynolds number tested. Hama [7] presents a qualitative curve, reproduced in Fig. 15 of p_b/p_s versus Reynolds number based on the viewpoint of Holder and Gadd [8]. This figure shows the various shapes that the p_b/p_s curve can assume depending on the upstream boundary layer influence and location of transition region. Present results appear to follow a trend like the A curve while Ref. [1] tripped data follow a C type curve. It can be concluded that the lowest Reynolds numbers tested here produced transitional flow over the base, but fully turbulent flow was evident for the higher values ($Re_\infty > 20 \times 10^6$).

The Korst theory line is shown in Fig. 14 for comparison. This theory is based on a two-dimensional, isoenergetic, back step geometry [9]. Also, the approach boundary layer is assumed very small compared to the step height which makes the solution a function of Mach number only for turbulent flows. The experimental model used here appears to satisfy the Korst assumptions at the highest Reynolds number value ($Re_\infty = 41 \times 10^6$), but the experimental data fall below the theory line. Figure 16 shows the trend of the Korst theory with Mach number. Also shown are the extensive results of Goin [10] which were used to support Korst's theory. The dashed line represents the summary data discussed by Nash and is the lower limit of p_b/p_s for thin approach boundary layers [11]. The IITRI high Reynolds number point falls very close to the lower limit line and is thus within the expected envelope of pressure ratios. In this particular case, the measured pressure ratio tends to substantiate Nash's recompression criteria.

Wall Pressure Measurements

A section of the wind tunnel side wall behind the model was instrumented with 45 pressure taps. The location of these taps is shown in Fig. 17. The results for 3 Reynolds numbers are presented in Fig. 18. The data are plotted along 4 rows of

pressure taps parallel to the model x-axis. Figure 18(a), (b), and (c) show Reynolds numbers increasing from 6.5 to 41 x 10^6. In order to adequately visualize the flow pattern which is causing the pressure variations, three shadowgraph photos are presented in Fig. 19. The photos show that the lip shock wave crosses only row II of the pressure taps. Examination of Fig. 19(a), (b) and (c) shows that the lip shock crosses row II at the third tap in all cases. Note that the apparent thickness of the model increases due to light beam distortion as Reynolds number increases. Unfortunately, the cross over is not defined in Fig. 18 because of the relatively thick tunnel wall boundary layer. This tends to smear the pressure rise across the lip shock due to the shock wave-boundary layer interaction on the tunnel wall. Qualitatively, row II does show an increase in pressure in the region of the first and second taps. It should be noted that the shadowgraph field of view included only the first 6 taps in each row.

In Fig. 18, the X value is the base pressure ratio measured along the model z-axis. It can be seen that the values of row I are essentially constant for all three Reynolds numbers. These values indicate that the flow has expanded uniformly over the measured distance but still has higher pressure than the base value. Row II shows that the flow over-expands to lower than the base pressure and then increases through the lip shock wave as the base is approached. Row III is an apparently unstable region at the outer edge of the central turbulent wake. Row IV along the x-axis shows continually increasing pressures in the rearward direction. Finally, the assumption of constant pressure mixing appears to hold for regions close to the base in the recirculation zone. Row I cannot be included here because it is in the expanding flow region. Also, the lip shock strength is finite and does cause some recompression of the over-expanded shear flow.

Fluctuating Pressures

The fluctuating pressure data exhibited unusual results. Initial conversion of RMS voltage readings to pressures gave extremely high values for the small transducers. Figure 20 shows the RMS pressure levels for several gauges. The 0.007 q_∞ line corresponds to typical fluctuating pressure levels for a subsonic boundary layer. Supersonic boundary layers would have smaller values (0.0013 q_∞) [12]. It is evident that all of the miniature gauges were reading from one to two orders of magnitude above the reference line. Although the larger gauges were reading much closer to the reference line, their trend with chamber pressure (or Reynolds number) was erratic. A noticeable change with chamber pressure was the reduced values at 165 and 345 psia (114 and 238 N/cm^2). These chamber pressures corresponded to an unchoked stagnation pressure control valve. For the 165 psia (114 N/cm^2) pressure only a different storage tank was used with a maximum of 250 psia (173 N/cm^2). A further indication that the control valve was affecting the readings was that the RMS levels dropped off sharply during the middle of a 275 psia (190 N/cm^2) run. It was concluded that the control valve became unchoked during a run due to the drop off in storage supply pressure. To determine if the large noise signals were acoustic or structural phenomena, the base plate was removed from the model and clamped directly to the outside of the wind tunnel. A metal to metal clamped contact was made. Figure 21 shows the resulting spectra for a miniature gauge mounted near the center of the base plate and choked control valve conditions. The spectrum for the Mach 2.97 flow condition had a strong peak at 2500 Hz and rapid drop off at higher frequencies which did not seem typical for a boundary layer type flow. The spectrum with the base mounted outside the tunnel showed the same strong peak at about 2500 Hz and similar behavior at other frequencies. The overall RMS voltage level outside the tunnel was almost the same as that inside. Therefore, the gauge was responding to vibrations or acoustic noise much more than it was responding to fluctuating pressures.

To determine whether the response was structural or acoustic, the base plate was supported on a 3 in. (7.62 cm) thick foam rubber pad sitting on a stand next to the test section. RMS voltage levels were recorded using the same gain settings as before. For this mounting configuration the signals were negligibly small. Therefore, the transducers did not respond to the acoustic noise outside the tunnel. It was concluded that the miniature transducers were responding mainly to wind tunnel vibration. The gauges were mounted rigidly in the base plate with conducting epoxy for good electrical contact. Also, the model was rigidly mounted against the tunnel wall so that the transducers felt any vibrations of the tunnel. Apparently, the choked control valve operation caused additional disturbances to be transferred to the test section structure. The technique of mounting two PZT discs back to back did not reduce their sensitivity to accelerometer effects as had been expected.

The larger gauges [D = 0.062 in. (0.157 cm)] had a much greater response to a given pressure signal than did the miniature gauges. The most useful results are for the unchoked control valve conditions, and these are plotted on Fig. 22 for the large gauges. The 0.007 q_∞ line is shown only as a reference since it is based upon free stream conditions. However, the subsonic boundary layer seen by gauge #6 is determined basically by the recirculation conditions. Gauge #6 does show the same trend with increasing total pressure as the reference line. The shoulder transducers are immersed in a supersonic boundary layer and should see fluctuating pressures on the order of 0.0013 q_∞. The recorded values for gauges 11 and 12 are substantially higher than the 0.0013 q_∞ line. Again, there appears to be a strong signal input to the transducers in addition to the normal fluctuating pressure signal. Therefore, even for the large gauges and the unchoked control valve conditions, the tunnel vibration is seriously affecting the gauge readings.

Figure 23 shows the spectral distribution for a large gauge (#6) on the base plate for several chamber pressures. The only unchoked control valve pressure is 345 psia (238 N/cm^2). The strong peaks at 125 and 250 Hz are from stray electronic signals picked up and amplified by the transducer charge amplifiers and could be filtered out. Another peak is evident at 800 Hz and from 2000 Hz to higher frequencies all four total pressures give approximately the same spectra. Since there is very little basic difference between the spectra for choked or unchoked control valve conditions, the vibration influence must still be strong even for unchoked valve runs.

Pressure Correlations

If the model vibration completely overwhelmed the pressure signals on the miniature transducers, the outputs of two gauges would be very well correlated. Figure 24 shows this to be true for several gauge combinations and choked control valve runs. The correlation coefficient $r(\eta,\tau)$ is between 0.85 and 1.0 at $\tau = 0$ for all cases. The $r(\eta,\tau)$ variation for two gauges mounted outside the tunnel shows similar behavior. Therefore, it is not possible to obtain correlation information for the choked valve runs.

Figure 25(a) shows the correlation between two large gauges (#11 and #12) on the shoulder for an unchoked condition. The coefficient, r, does not peak at $\tau = 0$ nor is it almost equal to one. Since the transducers are 3 to 4 boundary layer thicknesses apart, a correlation coefficient of less than one could be expected. The computed convection speed ratio (0.39) is rather low, but the data scatter and tape recorder zero shift could account for this. Therefore, the large gauges appear to give some pressure information for these conditions. Figure 25(b) shows the correlation coefficient between gauges #11 and #6 where gauge #11 is on the model shoulder and gauge #6 on the base. The curve peaks at zero time delay and has a maximum

correlation coefficient of only 0.13. The low value of $r(\eta,\tau)$ indicates that the model vibration component of the signals is not nearly as significant as shown in Fig. 24. But, still the peak is found at zero time delay indicating no convective process. The conclusion to be reached here is that the upstream shoulder boundary layer fluctuations are not a major influence on the base turbulence levels.

Unfortunately, there was only one large transducer located on the base plate so that correlations between two large gauges on the base plate were not possible. However, some correlations can be made with the miniature gauges by using a technique presented by L. N. Wilson in Ref. [13]. The technique assumes that two gauges receive signals which have two components. One component (the vibration signal) is seen by both gauges and is completely correlated. The other component (pressure signal) is random and uncorrelated between the two gauges. This second condition requires that the gauges be far apart so that a pressure signal is not common to both. Let the correlated signals be X and the uncorrelated ones be Y, then the total signal at gauge a is

$$S_a = X_a + Y_a$$

and similarly for gauge b. If these signals are subtracted, squared, and averaged, the result is

$$V = \overline{X_a^2} + \overline{Y_a^2} + \overline{X_b^2} + \overline{Y_b^2} - 2\overline{X_aX_b} - 2\overline{Y_aY_b}$$

assuming that cross products of X and Y are zero since they come from independent sources. Also, the mean square vibration and pressure signals are assumed to be constant at the two gauges, then

$$\overline{X_a^2} = \overline{X_b^2} = \overline{X^2}$$

$$\overline{Y_a^2} = \overline{Y_b^2} = \overline{Y^2}$$

Substituting,

$$V = 2\overline{X^2}\,[1 - r(\eta,\tau)_p] + 2\overline{Y^2}\,[1 - r(\eta,\tau)_v]$$

where $r(\eta,\tau)_p = \overline{X_a X_b}/\overline{X^2}$ is the correlation coefficient for the uncorrelated (pressure) signal, and $r(\eta,\tau)_v = \overline{Y_a Y_b}/\overline{Y^2}$ is the correlation coefficient of the correlated (vibration) signal. For complete correlated vibration signals $r(\eta,\tau)_v \simeq 1$, and for completely uncorrelated pressure signals $r(\eta,\tau)_p = 0$. Then, $V = 2\overline{X^2}$. Or, if the pressure signals are also well correlated, $V \simeq 0$ (very small compared to $\overline{X^2}$). This technique was used for gauges #2 and #4 on the base plate for an unchoked control valve run. Figure 26 shows the unmodified spectra of these two gauges. To utilize the above equations, the two signals must be made equal. Therefore, the power level of gauge #4 was amplified in each one-third octave bandwidth to force this gauge to have the same spectrum as gauge #2. The result of subtracting and squaring the modified gauge #4 signal from gauge #2 is shown in Fig. 27. The two strong peaks at 125 and 250 Hz are smoothed out considerably. These peaks were stray electronic noise which was accidentally picked up on this run. The 60 Hz peak still remains indicating that only one of the two charge amplifiers had recorded any 60 cycle noise. The 800 Hz peak indicates that one component of the signal is partially uncorrelated. It is significant that at 10,000 Hz and above, the $(S_a - S_b)^2$ signal is about twice that of the original S_a^2 signal. This means that the pressure correlation coefficient is nearly zero in this range. To check this result, a correlation measurement was made for the two separate signals with a one-third octave bandwidth at 10,000 Hz. Indeed, Fig. 28 does show that $r(\eta,\tau)$ is very small and there is no convection indicated. It should be noted that the positive $r(\eta,\tau)$ curve is symmetrical about $\tau = 10$ μS and not $\tau = 0$ as expected. This symmetry about $\tau = 10$ μS was also observed for other gauges with different

separation distances. A tape recorder zero shift of one of the channels is suspected for this anomaly. Using this signal subtraction technique with gauges #2 and #6 produces a similar result at the high frequency end of the spectrum.

Unfortunately, the relative magnitudes of the pressure and vibration signals cannot be determined by this subtraction technique. The technique cannot determine whether there is partial correlation of the pressure signal in the lower frequency range. In conclusion, the high vibration signals measured by the PZT transducers made analysis of fluctuating pressure information very difficult. Future use of the miniature transducers would require extensive modifications to the mounting method to eliminate vibration effects.

VELOCITY DATA

Mean Velocity Measurements

Mean velocity profiles were measured by hot wire traverses in the separated region close to the base plate. As mentioned previously, decreasing the free stream Reynolds number decreases the base density correspondingly and increases the inaccuracies of the hot wire readings. Further difficulties were encountered due to the intermittent nature of the wind tunnel operation. The procedure was to set the hot wires at a particular distance away from the base, make a run at a given density level, move the hot wires to another position, and rerun the same tunnel condition. Unfortunately, small changes in tunnel stagnation temperature and pressure can be reflected in large deviations in the hot wire reading due to the sensitivity of $\overline{E}$ to base density. Therefore, the scatter in the data is somewhat large. Figure 29 presents $\overline{U}$ as a function of axial distance out from the base plate for probe position 2P (see Fig. 3). The data at high Reynolds numbers indicate larger mean velocities than found earlier in Ref. [1].

Present data at the lower two Reynolds numbers is very erratic and cannot be used for quantitative results. The velocity distribution for the three probing positions at higher Reynolds numbers is shown in Fig. 30. The trend is very similar for all three positions. Assuming that a stagnation point is present on the base centerline, it could be expected that the mean velocities should decrease going from probe 2P to probe 6P. However, it must be remembered that the hot wire is not a directional sensor. Therefore, it can register horizontal as well as vertical velocity components. Close to the centerline, it is difficult to distinguish between vertical and horizontal reverse flow. Thus, the single hot wire measurements near the model centerline do not give an accurate representation of the developing vertical boundary layer.

Measurements taken with a cooled base plate proved unsuccessful because of the frost buildup on the model and the temperature corrections necessary to use wire calibrations which were made at room temperature. The results of a hot wire calibration curve are a function of the temperature difference between the wire and the surrounding air. When the base plate was cooled to 160°R (89°K), a steep temperature gradient was measured in the air adjacent to the base plate (as will be shown later). Therefore, the air temperature near the wire varied considerably as the base was approached. Efforts to compute the local temperature and then to correct the bridge voltage readings produced little improvement.

Fluctuating Velocities

The root mean square value of the fluctuating velocity component was derived from tape recordings of the fluctuating hot-wire bridge voltage, e'. Then,

$$e_{rms} = \sqrt{(\overline{e'^2})}$$

and

$$U_{rms} = \frac{1}{m} (e_{rms})$$

where m is the slope of the $\overline{E}$ versus $\overline{U}$ calibration curve at a particular $\overline{E}$ level. Figure 31 shows typical results for U_{rms} versus distance out from the base plate. The data of Ref. [1] are also presented and relatively good agreement is achieved. Turbulence levels are shown in Fig. 32. The values of turbulence intensity increase from 40 percent to over 100 percent as the base is approached. The Ref. [1] data also indicate the same trend of increasing turbulence intensity approaching the base, but the magnitudes are generally somewhat higher. Therefore, over the wide Reynolds number range from 4 to 40 x 10^6, the turbulence intensities in the base boundary layer are quite substantial.

The power spectral density results of the hot wire measurements are presented in the form of

$$\frac{(e_{rms\ 1/3})^2}{(e_{rms})^2\ \Delta f}$$

versus frequency f. Where

e_{rms} = rms value of fluctuating voltage over the complete frequency range

$e_{rms\ 1/3}$ = rms value of fluctuating voltage over a given 1/3 octave bandwidth

Δf = 1/3 octave bandwidth

Figure 33 shows typical spectra measured for several Reynolds numbers at an x distance of 0.028 in. (0.071 cm). The curves are nearly identical indicating that the spectrum does not change with Reynolds number. The slope of the log-log plot is -1.43 which is close to the -5/3 value expected for a turbulent attached boundary layer. Also, the distribution did not significantly change as base temperature was reduced to 160°R

(89°K). Figure 34 shows the change in the spectrum for several Reynolds numbers and different x distances. Again, the spectra are very much alike. The slope is again slightly less than -5/3 for the frequency range from approximately 1300 to 20,000 Hz indicating spectra similar to a normal attached boundary layer. The sharp increase in negative slope at about 25,000 Hz is caused by the drop off in frequency response of the tape recorder used. It should be noted that no unusual peaks are present in any of the power spectral density curves. Thus, it is assumed that the hot-wire geometry has no strong structural resonances, and the wind tunnel is free from predominant noise sources.

Velocity Correlations

Two hot wire probes were mounted in the transducer base plate through holes H1 and H2 to make correlation measurements. Hot wire probe H1 was set 0.03 in. (0.076 cm) from the base and not moved during the run series. Probe H2 was positioned at 0.29 in., 0.097 in., and 0.03 in. (0.74, 0.25, and 0.076 cm) out from the base. Both wires were set at the same distance as a check on the experimental results. The maximum correlation for equal distances would be at zero time delay. The data were analyzed with the IITRI Honeywell correlator.

Figure 35 shows plots of the correlation coefficient $r(\xi,\tau)$ versus time delay τ. The peak value of $r(\xi,\tau)$ for each separation distance is used to compute a convection speed toward the base plate. Figure 35(a) through (d) presents the results with increasing Reynolds number, and the convection speed computation is shown in each inset. It should be noted that the line connecting the two points does not necessarily pass through the origin. This may be due to a zero shift between the channels of the tape recorder or inaccuracies in fairing the curves to find the peak $r(\xi,\tau)$ value. The average convection speed

for all Reynolds numbers tested is 233 ft/sec (71 m/sec). All runs were made with the base plate at ambient temperature.

It can be concluded that the convection process near the base is not a function of Reynolds number. The convection velocity is slightly higher than the measured mean velocity [200 ft/sec (61 m/sec)] at the edge of the base boundary layer. Thus, velocity fluctuations near the centerline of the recirculation region must be convected toward the base at nearly mean recirculation flow velocities.

It is interesting to note that the computation of convection velocity using correlation techniques does not require any hot wire calibration whereas the measurement of mean velocity with one hot wire requires a painstaking calibration at controlled temperature and pressure conditions. Future measurements of mean recirculation velocities could be performed using two hot wires and correlation techniques instead of calibrating a single hot wire. The accuracy of the convection speed measurements was considerably better than the hot wire velocity profiles as Reynolds number was varied. Lower density flow did not effect the correlation technique. This method could also be made more accurate by using several separation distances. Wind tunnel time restrictions permitted only two separations for this test. Also, the convection in different directions could be obtained relatively easily. This technique can also be applied to much more complex flow fields.

Velocity-Pressure Correlations

Correlation measurements between a hot wire and a base plate transducer were inconclusive. Although most readings of correlation coefficient $r(\xi,\tau)$ were nearly zero, it could not be assumed that correlation was absent. Correlation coefficients between velocity and pressure fluctuations are typically small as shown in Ref. [14]. The large vibration signal from a transducer would not correlate with the hot wire signal since the

hot wires were not affected by vibration. However, a pressure signal which might have been correlated was probably so small that it could not be read.

TOTAL TEMPERATURE DATA

Three iron-constantan thermocouple probes were traversed in the recirculation region using the same three probing stations as the hot wires (2P, 4P, and 6P). The base plate was cooled to 160°R and 310°R (89°K and 172°K) as well as several runs at room temperature. When the base was at room temperature, it was actually warmer than the wind tunnel stagnation temperature since the air supply was stored outside.

Figure 36 shows how the recirculation to stagnation temperature ratio varies with base plate temperature, distance from base, and Reynolds number. As shown in Ref. [1] the recirculation temperature is very close to the free stream recovery temperature throughout most of the base flow region. The major drop in temperature occurs within 0.1 in. (0.25 cm) of the wall. There is a slight depression of the main recirculation temperature when the wall temperature is reduced from 310°R to 160°R (172°K to 89°K). Reference [1] explained this result as caused by the continual recirculation of cooled particles from near the wall into the region far removed from the wall.

Figure 36 also indicates the Reynolds number effect on the recirculation temperature. Far from the base plate wall, the Reynolds number has very little effect on T_B for a given base temperature. T_B drops off faster for low Reynolds numbers as the wall is approached. Then, the temperature gradient at the wall is smaller for low Reynolds numbers which is to be expected from heat transfer considerations. A comparison of the three thermocouple probe readings is shown in Fig. 37 where T_B/T_t is plotted against T_b/T_t. The probe readings are generally

very close together with the top probe reading (TC1) usually the lowest of the three. This figure is also used to compute the effective recirculation zone recovery temperature which is defined as the value of T_B when $T_b/T_t = 1$. An average value is found for all Reynolds numbers tested. Only measurements taken far from the base [x = 0.5 in. (1.27 cm)] are used for this computation. The data produce a linear increase of T_B with T_b so that $T_{Br}/T_t = 0.927$. Also, the slope of this line is useful in heat transfer calculations and is found to be 0.125. Figure 38 again shows a temperature ratio plot for one Reynolds number. This plot shows the deviation of T_B/T_t from the "far removed" linear relationship as the base is approached.

The results of the thermocouple probing experiments again show that a thermal boundary layer exists for all Reynolds numbers tested.

HEAT TRANSFER DATA

Since the wind tunnel flow was intermittent, a transient heat transfer measurement method was appropriate. The model was designed to measure the increase in heat capacity of the thin nickel base plate. Conduction losses to the interior of the model were minimized by mounting the nickel plate on a bakelite block. The heat transferred per unit area through the shear layer, recirculation zone, and base boundary layer to the base plate can be written as:

$$\frac{\dot{Q}}{A_{BP}} = \omega C_p g \frac{dT_b}{dt} \tag{11}$$

where $\dot{Q}$ = total rate of heat transfer to base plate
A_{BP} = area of base plate
ω = specific weight of nickel plate
C_p = specific heat of nickel plate
g = thickness of nickel plate

T_b = temperature of nickel plate
t = time

There are three heat transfer coefficients which can be defined for this problem. The first is a base plate film coefficient, h_{BP}:

$$\frac{\dot{Q}}{A_{BP}} = h_{BP} (T_B - T_b) \tag{12}$$

where T_B = recirculation zone temperature outside the base boundary layer. A total heat transfer coefficient and a shear layer coefficient are also of value.

$$\frac{\dot{Q}}{A_{BP}} = h_{TOT} (T_r - T_b) = h_{SL} (T_r - T_B) \tag{13}$$

and T_r = recovery temperature at the outside edge of the shear layer.

It should be noted that all three heat transfer coefficient definitions use the base area as the reference area. These definitions follow the development of Ref. [1] so that direct comparisons can be made with previous data. However, extreme caution must be exercised when comparing present data with theory or other experimental results. For example, many theories defining h_{SL} use a shear layer effective area as a reference.

Rewriting Eq. (11) with the definition for h_{TOT} gives

$$h_{TOT} (T_r - T_b) = \omega C_p g \frac{dT_b}{dt} \tag{14}$$

By assuming that T_r and h_{TOT} are constant over the temperature interval of a given run and writing dT_b/dt as $\Delta T_b/\Delta t$, Eq. (14) becomes

$$\frac{\Delta T_b}{\Delta t} = \frac{h_{TOT}}{\omega C_p g} (T_r - T_b)$$

Then, h_{TOT} can be derived from the slope of a plot of $\Delta T_b/\Delta t$ versus $(T_r - T_b)$. A typical plot used to determine h_{TOT} is shown in Fig. 39. This figure shows a good linear relationship over the whole run of 8 seconds. This result is for the highest tunnel Reynolds number and lowest initial base temperature. As Reynolds number decreases and at higher base temperatures, the accuracy of computing h_{TOT} decreases. Also, at lower Reynolds numbers the initial tunnel starting perturbation was much more significant, and linearity was not achieved for several seconds. The length of run at lower Reynolds number was 12 to 15 seconds.

Heat Transfer Coefficient

The array of 15 thermocouples used to measure the distribution of h_{TOT} on the base plate was shown in Fig. 8. The value of h_{TOT} computed from each gauge is shown on Fig. 40 for a particular high Reynolds number run. First, the heat transfer coefficient is not uniform in the spanwise direction indicating that some three-dimensional flow effects are present. For each horizontal row of 5 thermocouples, the h_{TOT} values appear to peak at the model y-axis. This is probably due to tunnel wall boundary layer effects. In the y-direction there is a definite decrease in h_{TOT} for the top row, thermocouples #1 to #5. This result corresponds to the physical interpretation shown in Fig. 41. A stagnation region with high heat transfer coefficient would be expected along the z-axis. The heating rate should then decrease in the y-direction as the flow accelerates and recirculates by entrainment of the free shear layer. However, the first two rows (TC11-15, and TC6-10) give nearly the same coefficient within the scatter of the data. This indicates that a stagnation region exists near the z-axis and the lower heating rates become pronounced as the base corner is approached. The results at low Reynolds number are not conclusive with respect to vertical variation of h_{TOT}.

Figure 42 shows results for the lowest Reynolds number tested. Here, the low values of h_{TOT} and small overall temperature rise produce a large variation from one thermocouple to another. Since the model was designed for the high heating rates, the accuracy necessarily suffers at low Reynolds number. Therefore, it is felt that the trend shown in Fig. 40 is correct and should apply throughout the Reynolds number range.

In order to evaluate the heat transfer coefficient trend with Reynolds number, an average value of h_{TOT} was computed for each run. This value was a simple arithmetic average of the 15 thermocouples. Figure 43 shows the results of h_{TOT} average versus Reynolds number. An attempt was made to determine the effect of the wet air supplied to the tunnel. The wind tunnel dryer could only be used for Reynolds numbers of 10×10^6 or less. Several runs were made with dry air, however, the results showed no significant effect so that no correction was made for the wet air supply. The results of Ref. [1] are also included for comparison in Fig. 43. The general trend of increasing h_{TOT} is carried out in the present results. A more meaningful comparison can be made by non-dimensionalizing the heat transfer coefficient to a Stanton number.

Total Stanton Number

The Stanton number based on h_{TOT} can be defined as

$$St_{TOT} = \frac{h_{TOT}}{(\rho \overline{U} C_p)_2}$$

where ρ, $\overline{U}$, and C_p are the air density, mean velocity, and specific heat evaluated at the outer edge of the shear layer (region 2, Fig. 41). The expansion process occurring at the corner is assumed to be isentropic. Since constant pressure mixing is assumed through the shear layer, the expansion proceeds from free stream static pressure to a value equivalent

to the base pressure. The Mach number in region 2 is then computed from the ratio of base to tunnel stagnation pressure. The lip shock wave is assumed to be of negligible strength. Hama's results [Ref. 7] indicate that this latter assumption may be questionable.

Figure 44 presents the results of St_{TOT} versus Reynolds number. Previous discussion has shown that the 300°R (167°K) base temperature data would be most valid. The straight line is drawn through the best 300°R (167°K) data. One point at low Reynolds number is extremely low and should be disregarded. The 400°R (222°K) data is apparently less accurate since it shows a trend of increasing St_{TOT} with Reynolds number which contradicts many previous theoretical and experimental results. The conclusion is that the 400°R (222°K) values are too low due to the increased experimental difficulties at low Reynolds numbers and higher base temperatures. The earlier data of Ref. [1] is also included for comparison.

Shear Layer Stanton Number

The theoretical development by Korst [Ref. 9] includes the prediction of a shear layer Stanton number, St_{SL}, for a two-dimensional back step geometry. In order to compare present results to the St_{SL} values predicted by Korst, it is necessary to compute h_{SL}. From Eqs. (12) and (13),

$$\frac{h_{TOT}}{h_{BP}} = \frac{T_B - T_b}{T_r - T_b} \qquad \frac{h_{TOT}}{h_{SL}} = \frac{T_r - T_B}{T_r - T_b} \tag{15}$$

Figure 37 shows that the relationship between T_B and T_b is nearly linear as T_B approaches T_r. Therefore, this linear relationship can be written as

$$T_B = T_r + \frac{\Delta T_B}{\Delta T_b}(T_b - T_r)$$

Then,

$$\frac{h_{TOT}}{h_{BP}} = 1 - \left(\frac{\Delta T_B}{\Delta T_b}\right)_{T_B = T_r} = 1 - 0.125 = 0.875 \quad (16)$$

where the value of $(\Delta T_B/\Delta T_b)_{T_B = T_r}$ is taken from Fig. 37. This development follows the presentation of Ref. [1], and the conclusion is similar: the heat flow resistance of the base boundary layer is the major resistance to heat flow (87 percent). It is possible to estimate the ratio of h_{TOT}/h_{SL} by using the series resistance concept for heat flow proposed by Page and Dixon [15],

$$\frac{1}{h_{TOT}} = \frac{1}{h_{SL}} + \frac{1}{h_{BP}}$$

Therefore,

$$\frac{h_{TOT}}{h_{SL}} = 1 - \frac{h_{TOT}}{h_{BP}} = 0.125 \quad (17)$$

These results hold over the complete Reynolds number range tested as shown in Fig. 37. It is now possible to compute St_{SL}:

$$St_{SL} = \frac{h_{SL}}{(\rho\bar{U}c_p)_2}$$

The denominator is evaluated at the outer edge of the shear layer. Figure 45 shows the plot of St_{SL} versus Reynolds number. Again the 300°R (167°K) data is thought to be most accurate.

The manipulations required to compare Korst's theory to the present results are somewhat complex so that an example is presented for clarity. For a $Re_\infty = 39.2 \times 10^6$ point the base to stagnation pressure ratio produced an M_2 value of 4.43. Korst's paper [9] presents a graphical selection for σSt_{SL} versus T_B/T_t with Crocco number squared as a parameter. T_t is the stagnation temperature in region 2. Korst's analysis

assumes that $T_B = T_b$ so that for comparison here the temperature of the recirculation region is used. For the lower base temperature $T_B/T_t \simeq 0.84$ and for $C_2^2 = 0.8$, Ref. [9] gives $\sigma St_{SL} = 0.062$. Since the present analysis is based upon the base plate area, a conversion of the Korst value must be made because it is based on an effective shear layer area. Previous measurements have been made with this model of the approximate position of the stagnation point in the reattachment region [1]. The value of A_{SL}/A_{BP} was 1.73 for a Reynolds number of 4×10^6. Unfortunately, this measurement has not been done at the higher Reynolds numbers so it must be assumed that the value is nearly constant with Reynolds number. Then the corrected Korst value of σSt_{SL} would be 0.107. Finally, results are plotted on Fig. 45 for σ's of 12, corresponding to subsonic jet spreading, and 24.2 which is found from the supersonic spreading equation:

$$\sigma = 12.0 + 2.76\, M_2 = 24.2$$

The data tend to cluster around the subsonic Korst theory rather than the supersonic values as might be expected. As suggested in Ref. [1], the above relation for σ was based on data for jets exhausting into still air which may not apply to base flow geometries.

SCALING EFFECTS

The present experiments have extended studies of base recirculation flow to a Reynolds number of 41×10^6. At this Reynolds number the flow has undergone a natural transition to turbulent flow and is not subjected to the disturbance of a boundary layer trip. The base pressure, which was decreasing rather sharply at the lower Reynolds number, has leveled off at the higher values of Reynolds number. The shadowgraph photos show the lip shock wave remains essentially stationary as the Reynolds number increases.

Convection speeds in the recirculation region measured close to the base plate show very little dependence on Reynolds number. Also, turbulence levels remain high as Reynolds number increases. The heat transfer results, presented in terms of the Stanton number, exhibit little change with increasing Reynolds number even though measuring inaccuracies produce a large spread in the data.

The extrapolation of data to full scale flight Reynolds numbers must now be considered. The Saturn V flight trajectory shows a Mach 3 velocity at about 79,000 ft (24 KM) altitude. Then, for a 350 ft (107 m) long vehicle the length Reynolds number would be approximately 3×10^8. Therefore, present test results would have to be extrapolated nearly one order of magnitude to produce flight values.

The geometry of the present model was very simple in order to understand basic flow phenomena. The first obvious difference from the flight vehicle is two-dimensional versus axisymmetric geometry. Figure 46 shows a comparison of two dimensional theory by Korst [9] with the axisymmetric theory of Zumwalt [16] and the present base pressure data. The Zumwalt theory would apply to a blunt-based cone-cylinder geometry which would represent the Saturn V with the engines off. Model

tests of the Saturn V have presented base pressure data for jet off and jet on [17]. Figure 47 shows the comparison between the model test data and Zumwalt's theory. The theory compares fairly well with the jet off data beyond the transonic flight regime. As expected, the jet on data exhibits completely different characteristics at the higher Mach numbers due to the complex plume and free stream flow interactions. The conclusion must be that the simplified flow picture of Zumwalt can only be applied to jet off models. Similarly, the present two-dimensional experimental results should only be used as a guide for understanding simple recirculating flow phenomena.

Finally, it should be noted that turbulent flow involves the transport of mass, momentum, and energy by large scale fluid interchange. The motion of eddies and transport of vorticity are basically three-dimensional phenomena so that it is difficult to obtain a truly two-dimensional turbulent flow.

CONCLUSIONS

Measurements of static and fluctuating pressures, mean and fluctuating velocities, and velocity correlations, total temperature, and heat transfer were made in the separated flow region behind a two-dimensional, blunt base model. Tests were made at Mach 2.97 and a Reynolds number range of 6.5 to 41 x 10^6 based on model length. The major results were:

1. Turbulence intensities of 40 to 100 percent were found in the recirculating velocity field close to the base. Convection speeds perpendicular to the base were measured using correlation techniques between two hot wires. Measurements showed convection speeds of approximately 200 ft/sec (61 M/sec) directed toward the base near the model centerline. These values did not vary appreciably with Reynolds number. The correlation technique is quite accurate compared to the use of one calibrated hot wire for mean flow measurement particularly at low density.

2. Spectral analysis of hot wire signals indicates a typical turbulent boundary layer spectrum with slightly less than a -5/3 decay from a frequency of 1300 Hz to the tape recorder cut off frequency. No unusual peaks were observed in the power spectral density plots.

3. Base pressure measurements at high Reynolds numbers corresponded to data presented by Nash for very thin shoulder approach boundary layers.

4. Difficulties were encountered with fluctuating pressure measurements because of the sensitivity of the lead-zirconate-titanate transducers to wind tunnel and model vibrations. Choked flow through the wind tunnel stagnation pressure control valve produced exceptionally high vibration levels. For this tunnel condition, the pressure signal output from both the large [0.062 in. (0.158 cm) diam.] and miniature [0.025 in. (0.0635 cm) diam.] transducers was overwhelmed by the vibration signal. However, for an unchoked control valve condition (highest Reynolds number), the vibration level was reduced so that some correlation information could be derived from the large gauges. It was found that disturbances in the upstream shoulder boundary layer were not correlated with base plate fluctuations. The output from the miniature gauges was still primarily due to vibration even at the unchoked valve condition. It is believed that the large gauges could be much more accurate in future tests if a vibration isolating mount was used.

5. Total temperature measurements in the recirculation region showed that the major portion of the flow possessed a temperature slightly less than free stream recovery temperature. Close to the base, a thermal boundary layer was evident when the base was cooled below ambient temperature. The recirculation temperature far from the base was not affected by Reynolds number variations.

6. The base boundary layer acts as the major resistance to heat flow from the free stream. This boundary layer represents 87 percent of the heat flow resistance where the shear layer is only 13 percent.

7. The Stanton number, representing the total heat transfer coefficient, is not significantly affected by Reynolds number variation.

8. The shear layer heat transfer coefficient has been compared to Korst's theory. The agreement is better when the incompressible value of σ is used. The Mach number dependence of σ was based on jets exhausting into quiescent air and may not be applicable for the present geometry.

RECOMMENDATIONS

Further work is needed in several specific areas. An axisymmetric base flow model would better represent a flight vehicle. Also, the recirculation region could be instrumented judiciously using past results as a reference. The final step would be to instrument a model which had exhausting jet plumes. The techniques derived for the present model using miniature hot wire probes could then be applied to a more complex flow pattern. Appropriate mounting of pairs of hot wire probes would give accurate measurement of convection speeds. This method proved very satisfactory in the present tests and does not rely on calibrations of hot wires at low density. Also, it would be advantageous to use a facility with heated gas capabilities such as the NASA Marshall, Thermo-Acoustic Jet Facility. A heated flow would eliminate the requirement for liquid nitrogen cooling inside the model. Therefore, frost buildup on the base plate and liquid nitrogen leakage would be eliminated. Heat transfer measurements would involve a temperature difference from the heated gas to the ambient temperature base plate. The cooled hot film probes could also be used for velocity measurements in a recirculating hot gas flow if necessary.

Additional research with the larger [0.062 in. (0.158 cm) diameter] PZT gauges could provide a useful fluctuating pressure measuring device. The miniature gauges [0.025 in. (0.0635 cm) diameter] may be too susceptible to vibration for any continuing effort. However, the higher output of the large gauge could be sufficient if adequate vibration isolation were provided. Some simple test techniques could be developed to assure good vibration isolation before installation in a wind tunnel.

Basic flow research could be continued with the present model or future axisymmetric models. The lip shock wave strength and position could be studied more accurately by sucking off the wind tunnel wall boundary layer ahead of the measuring station. Finally, shear layer velocity profile measurements could be used to define δ more accurately.

REFERENCES

1. Krause, F.R., Dahm, W.K., Larson, R.E., and Hanson, A.R., "Convective Heat Transfer in Turbulent, Supersonic Base Flow," NASA TMX-53462, April 1, 1966.

2. Domich, E.G., Jantscher, H.N., and Olson, D.N., "Aeronautical Research Facilities," RAL Res. Rep. No. 152, Rosemount Aeronautical Laboratories, Minneapolis, Minn., September 1958.

3. Clinch, J.M., "Study of Vibrations Induced in Thin-Walled Pipes under Varying Flow Conditions," Final Report, IIT Research Institute, Contract No. NAS8-20325, June 1967.

4. King, L.V., "On the Convection of Heat from Small Cylinders in a Stream of Fluid," Phil. Trans. Roy. Soc. London, Vol. 214A, pp. 373-432, 1914.

5. Davies, P.O.A.L., and Fisher, M.J., "Heat Transfer from Electrically Heated Cylinders," Proceedings of the Royal Society, A, Vol. 280, pp. 486-527, 1964.

6. Eckert, E.R.G., and Drake, R.M., Heat and Mass Transfer, McGraw-Hill Book Co., New York, 1959.

7. Hama, F.R., "Experimental Investigations of Wedge Base Pressure and Lip Shock," TR No. 32-1033, Jet Propulsion Laboratory, Pasadena, Calif., Dec., 1966.

8. Holder, D.W., and Gadd, G.E., "The Interaction between Shock Waves and Boundary Layers and Its Relation to Base Pressure in Supersonic Flow," in Boundary Layer Effects in Aerodynamics, Philosophical Library, New York, 1955.

9. Korst, H.H., Chow, W.L., and Zumwalt, G.W., "Research on Transonic and Supersonic Flow of a Real Fluid at Abrupt Increases in Cross Section," University of Illinois, Engineering Experimental Station, ME Tech. Rep. 392-5, Oct. 1964.

10. Goin, K.L., "Effects of Plan Form, Airfoil Section, and Angle of Attack on the Pressure Along the Base of Blunt-Trailing-Edge Wings at Mach Numbers of 1.41, 1.62, and 1.96," NACA RML 52D21, 1952.

11. Nash, J.F., "A Discussion of Two-Dimensional Turbulent Base Flows," National Physical Laboratory Aero Report 1162, July, 1965.

REFERENCES (Cont'd)

12. Speaker, W.V., and Ailman, C.M., "Spectra and Space-Time Correlations of the Fluctuating Pressures at a Wall Beneath a Supersonic Turbulent Boundary Layer Perturbed by Steps and Shock Waves," NASA CR-486, May, 1966.

13. Wilson, L.N., "An Experimental Investigation of the Noise Generated by the Turbulent Flow Around a Rotating Cylinder," Institute of Aerophyaics, University of Toronto UTIA Report No. 57, April, 1959.

14. Serafini, J.S., "Wall-Pressure Fluctuations and Pressure-Velocity Correlations in Turbulent Boundary Layers," North Atlantic Treaty Organization, Report 453, April 1963.

15. Page, R.N. and Dixon, R.J., "Base Heat Transfer in a Turbulent Separated Flow," The Boeing Company, Document D2-20191-1, 1963.

16. Zumwalt, G.W., "Analytical and Experimental Study of the Axially-Symmetric Supersonic Base Pressure Problem," Ph.D. Dissertation, Dept. of Mechanical Engineering, University of Illinois, 1959.

17. Wasko, R.A., "Wind-Tunnel Investigation of Thermal and Pressure Environments in the Base of the Saturn S-IC Booster from Mach 0.1 to 3.5," NASA TN D-3612, September, 1966.

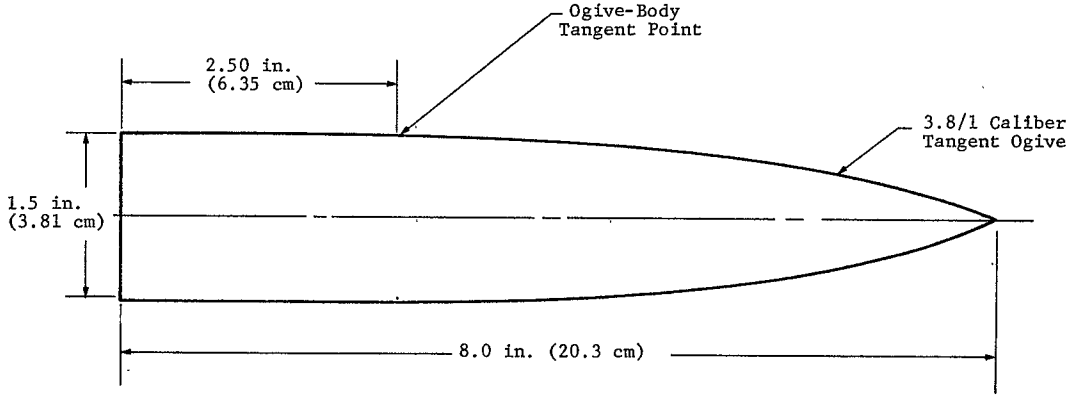

Fig. 1. WIND TUNNEL MODEL CROSS-SECTIONAL DIMENSIONS

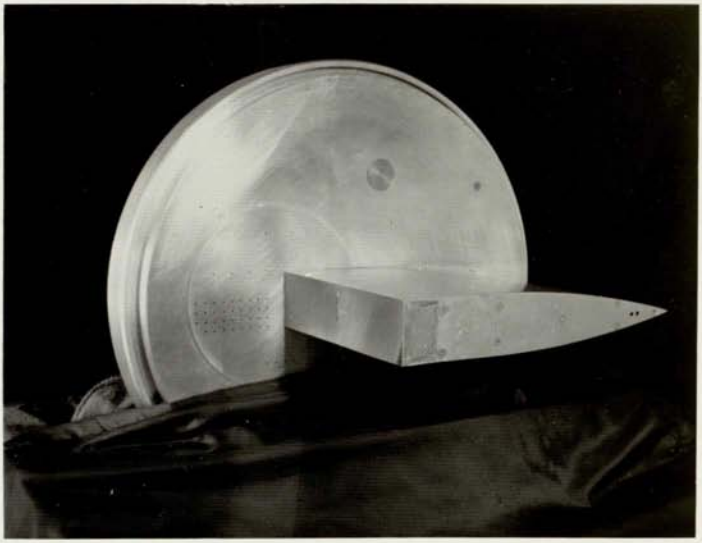

Fig. 2. MODEL INSTALLATION ON REMOVABLE WIND TUNNEL WALL SECTION

NOT REPRODUCIBLE

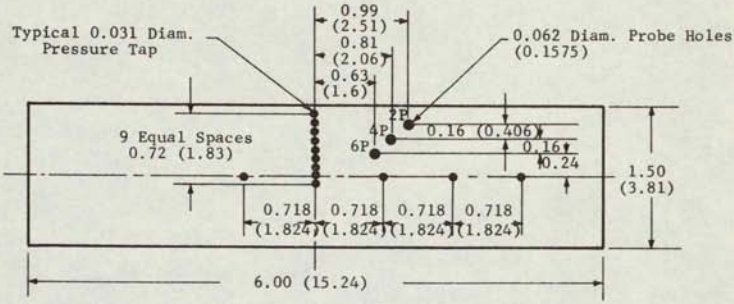

Dimensions are in Inches and (Centimeters)

(a) Probing Base Plate, 0.062 in. (0.1575 cm) Stainless Steel

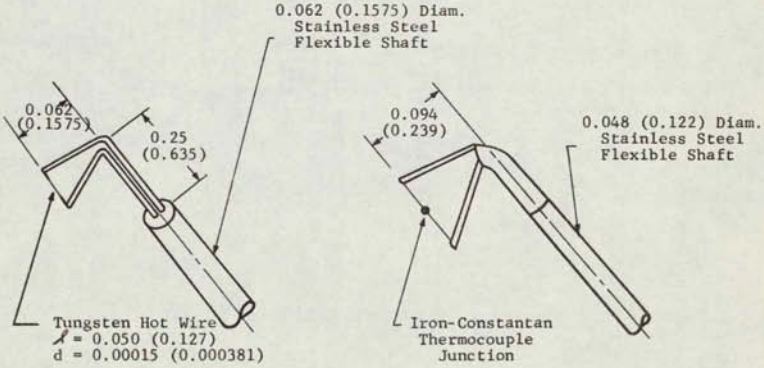

(b) Hot Wire Probe

(c) Thermocouple Probe

Fig. 3. PROBING BASE PLATE CONFIGURATION

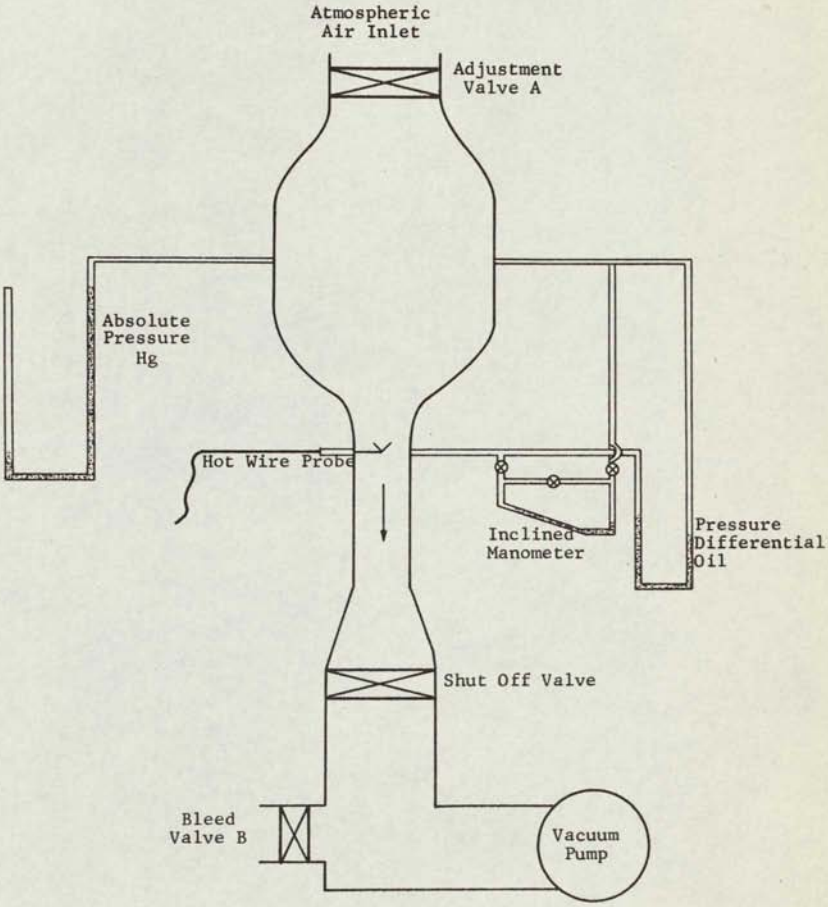

Fig. 4. LOW DENSITY CALIBRATION APPARATUS

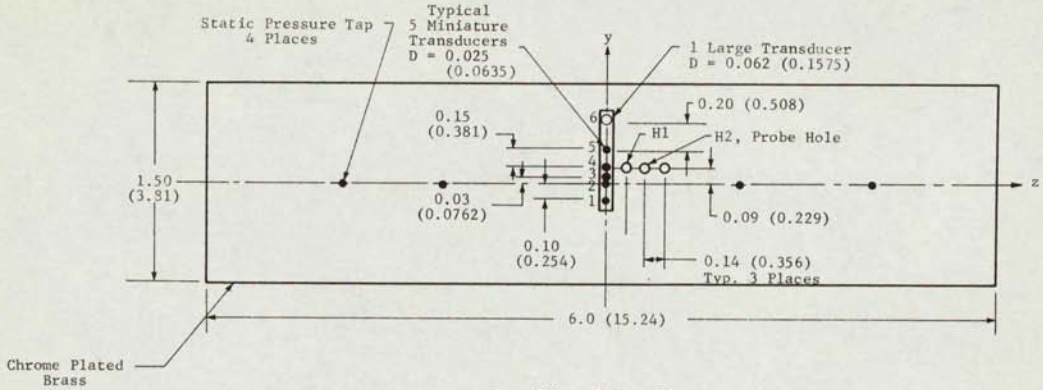

Rear View of Base Plate

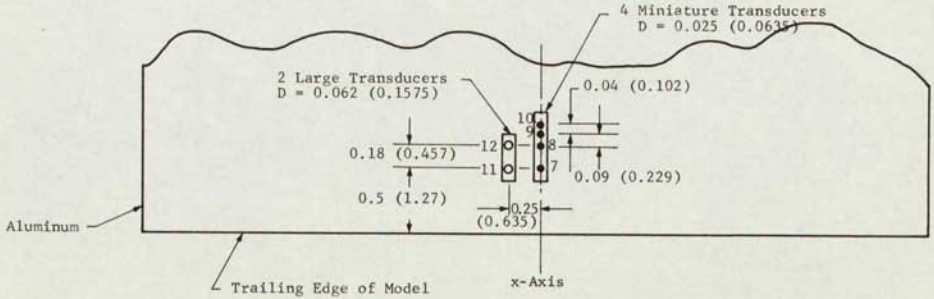

Dimensions in Inches and (Centimeters)

Plan View of Model

Fig. 5. TRANSDUCER BASE PLATE AND SHOULDER SECTION

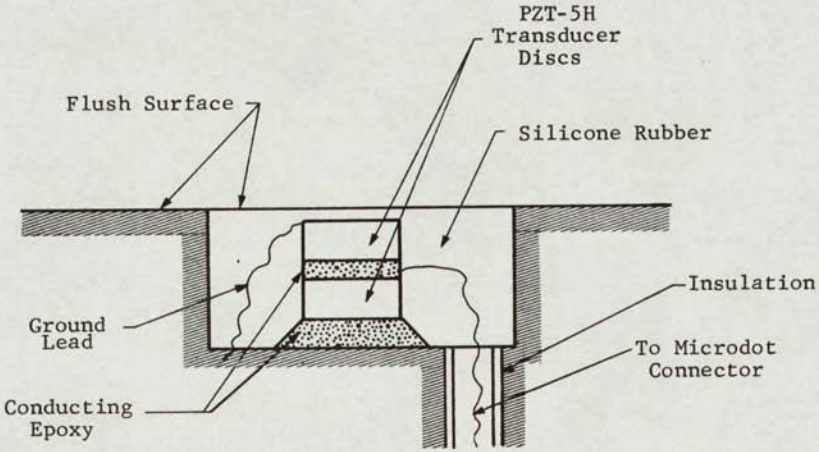

Fig. 6. SCHEMATIC OF TRANSDUCER INSTALLATION

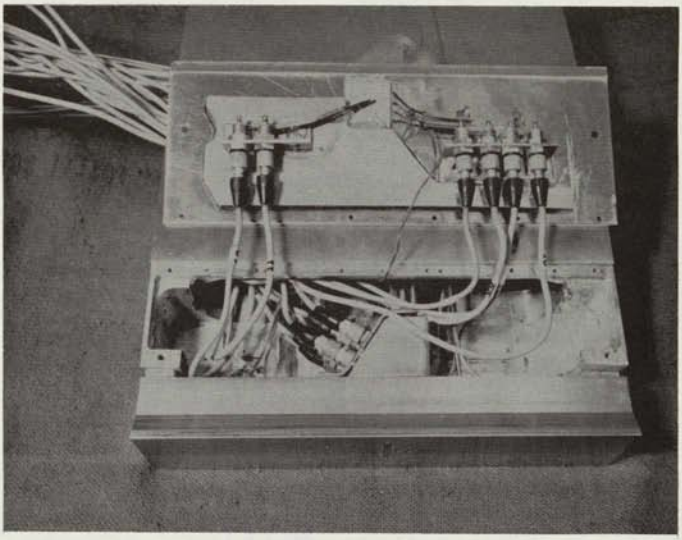

Fig. 7. VIEW OF TRANSDUCER BASE PLATE INSTALLED IN MODEL WITH COVER PLATE REMOVED

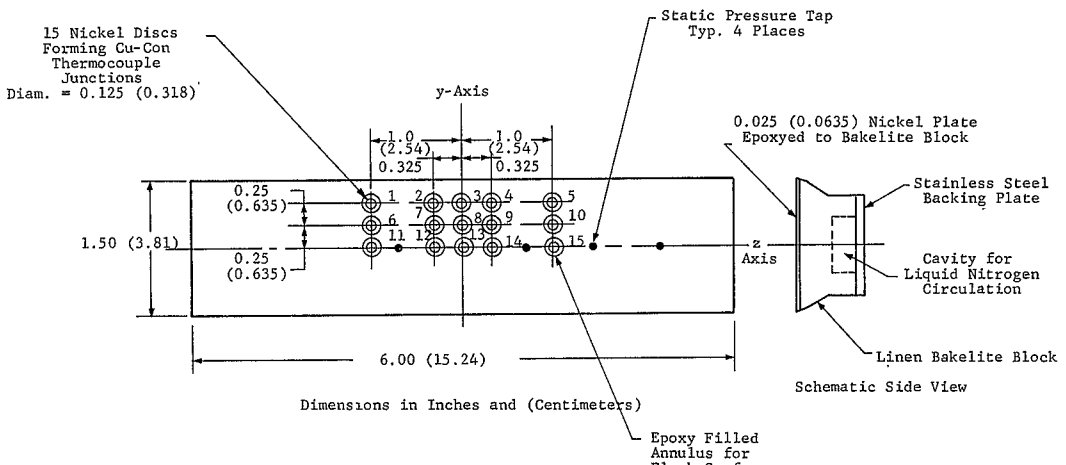

Fig. 8. HEAT TRANSFER BASE PLATE

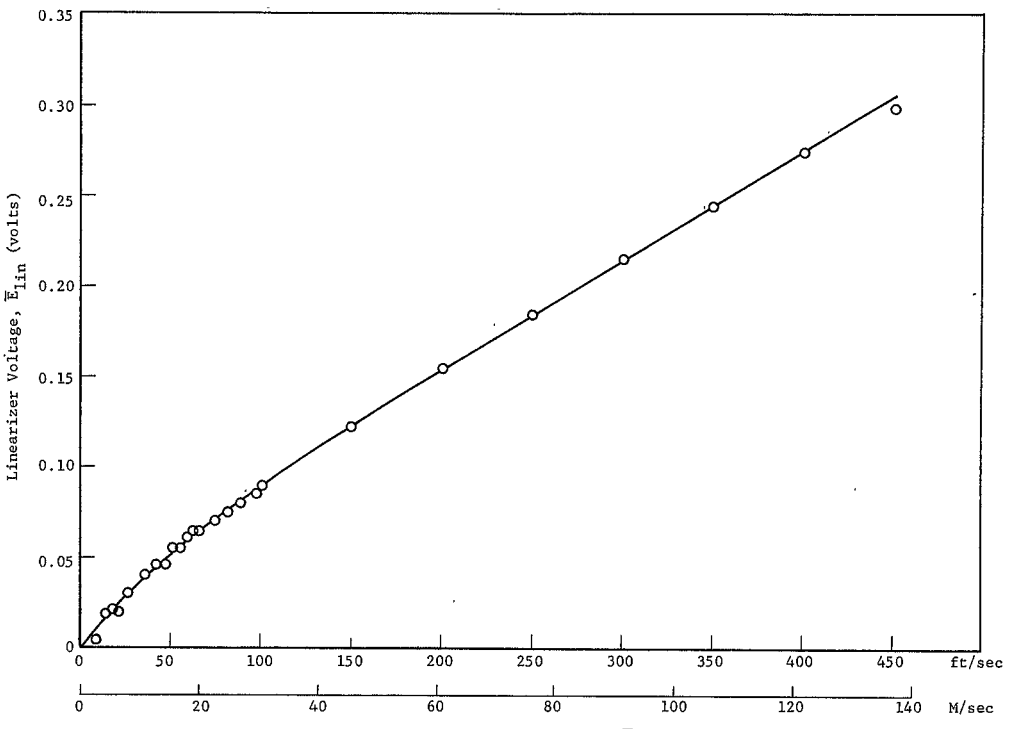

Fig. 9. LINEARIZER OUTPUT VOLTAGE VS MEAN AIR FLOW VELOCITY AT ATMOSPHERIC PRESSURE

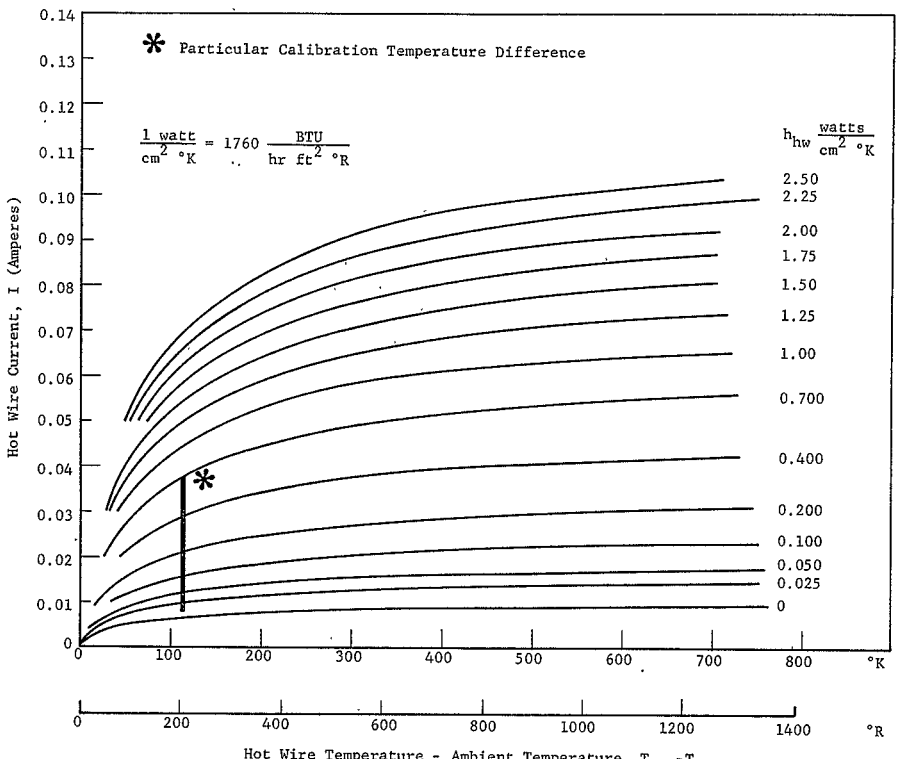

Fig. 10. HOT WIRE CURRENT VERSUS TEMPERATURE DIFFERENCE, $T_{hwm}-T_o$, FOR VARIOUS VALUES OF HEAT TRANSFER COEFFICIENT. Wire Diameter d = 0.00015 in. (0.000381 cm), Wire length, ℓ = 0.050 in. (0.127 cm).

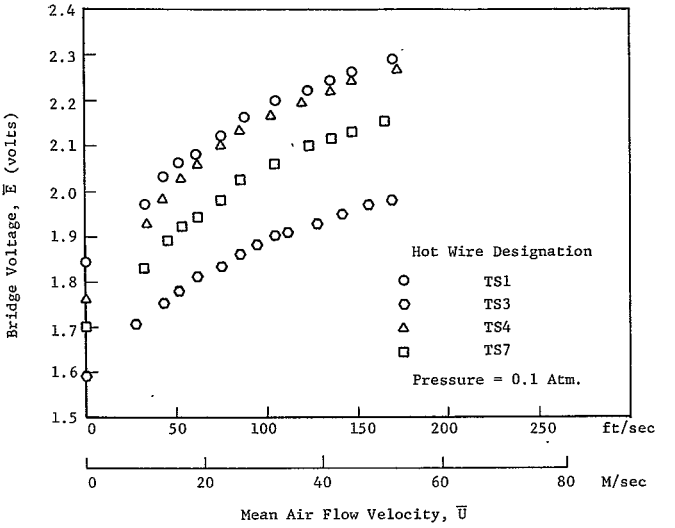

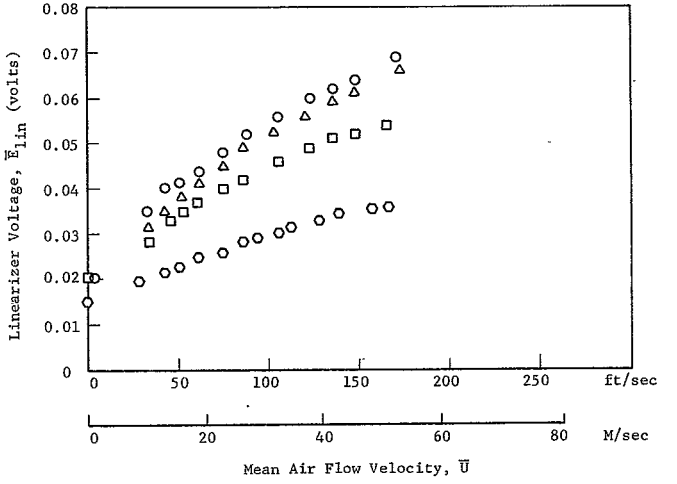

Fig. 11. BRIDGE VOLTAGE AND LINEARIZER VOLTAGE VERSUS MEAN AIR FLOW VELOCITY AT 0.1 ATMOSPHERE PRESSURE

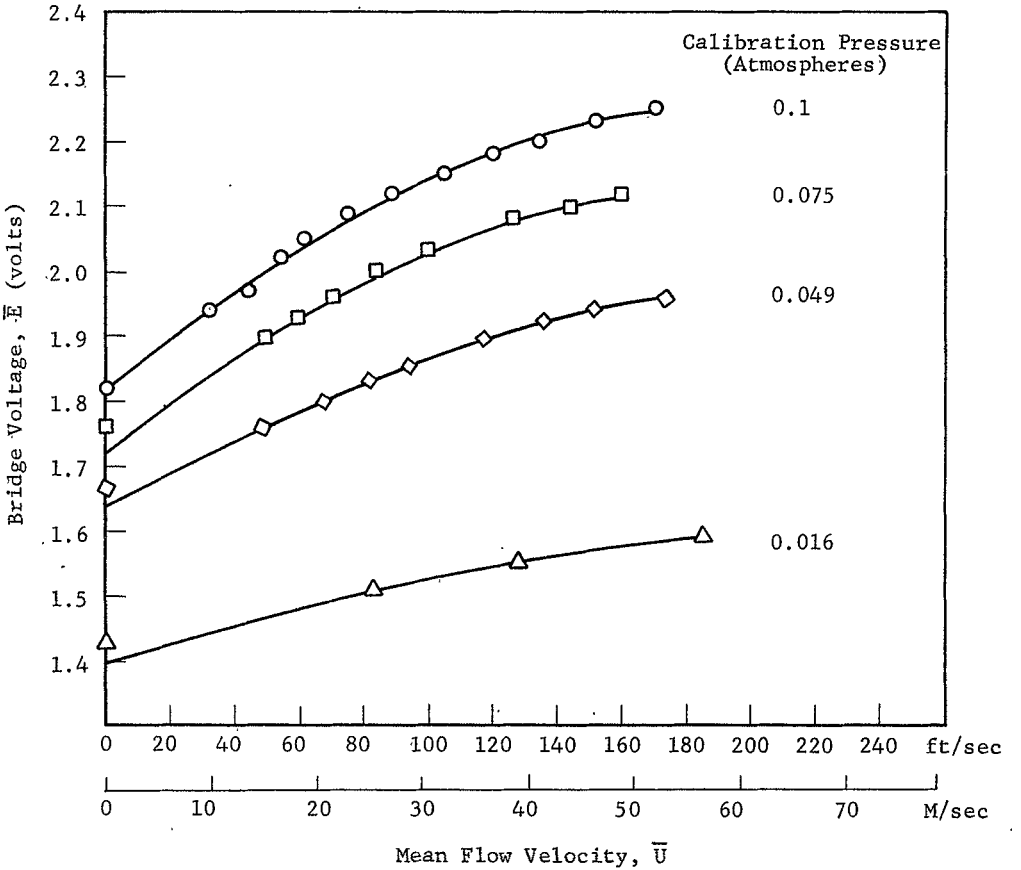

Fig. 12. CALIBRATION OF HOT WIRE PROBE TS4 AT FOUR PRESSURE LEVELS

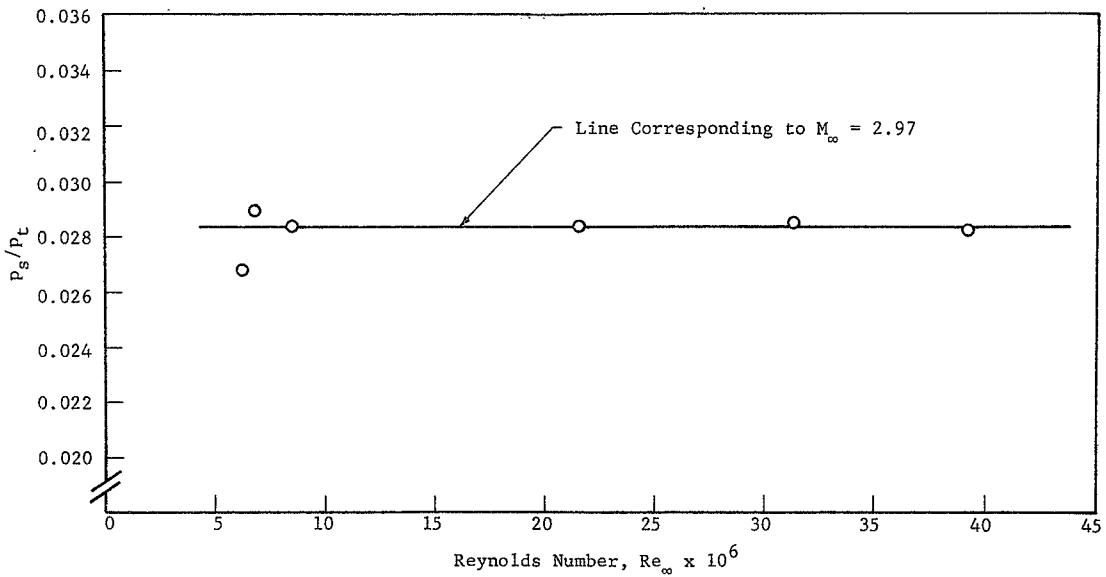

Fig. 13. SHOULDER TO TOTAL PRESSURE RATIO VS REYNOLDS NUMBER USED TO COMPUTE MEAN TUNNEL MACH NUMBER

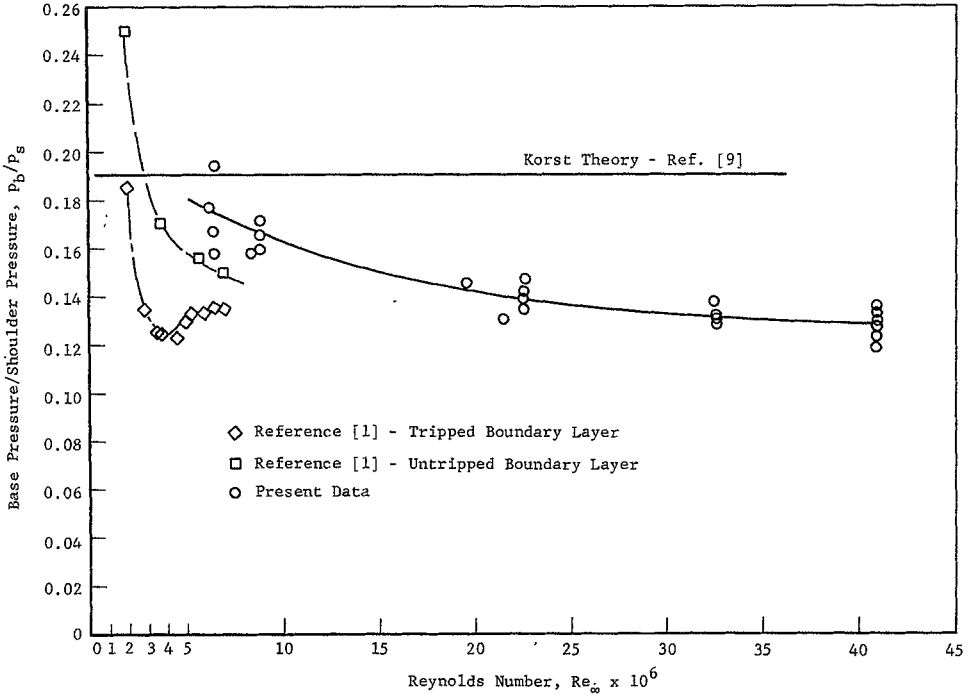

Fig. 14. BASE TO SHOULDER PRESSURE RATIO VS REYNOLDS NUMBER AT $M_\infty = 2.97$

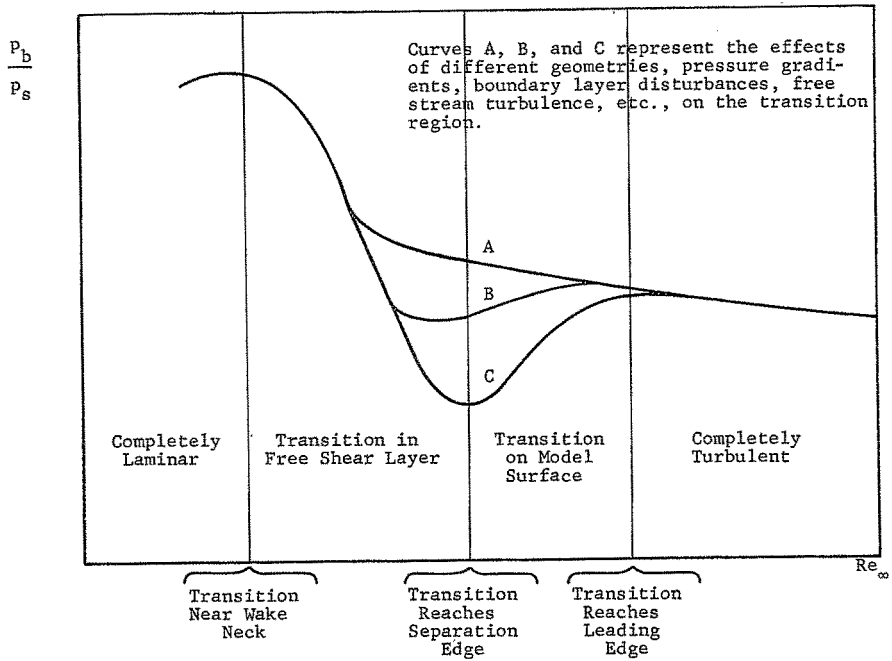

Fig. 15. QUALITATIVE SHAPE OF p_b/p_s CURVE AS REYNOLDS NUMBER VARIES. From Hama Reference [7].

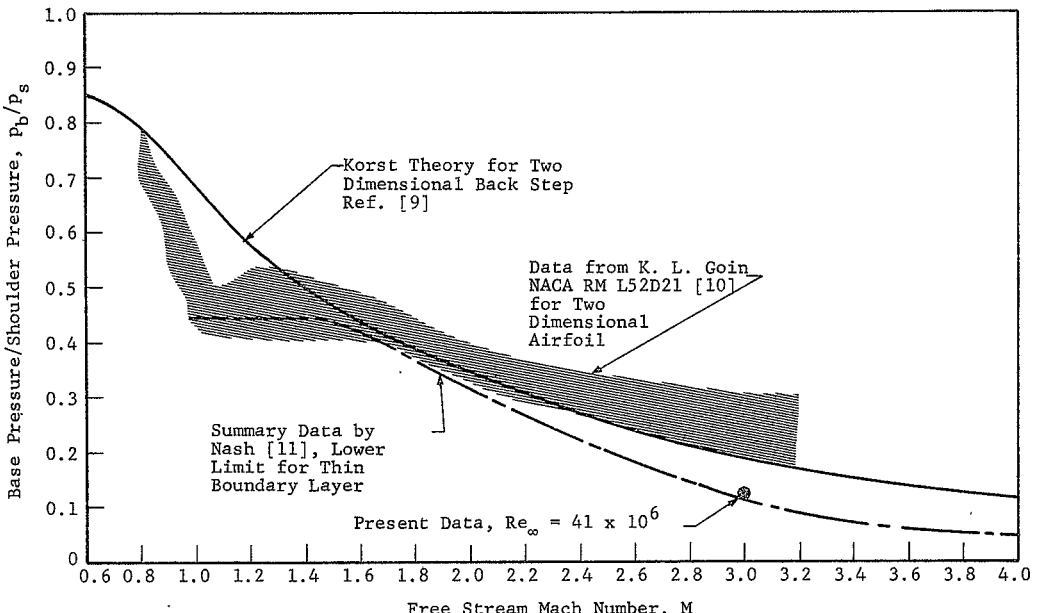

Fig. 16. COMPARISON OF MEASURED BASE PRESSURE RATIO VERSUS MACH NUMBER WITH PREVIOUS RESULTS.

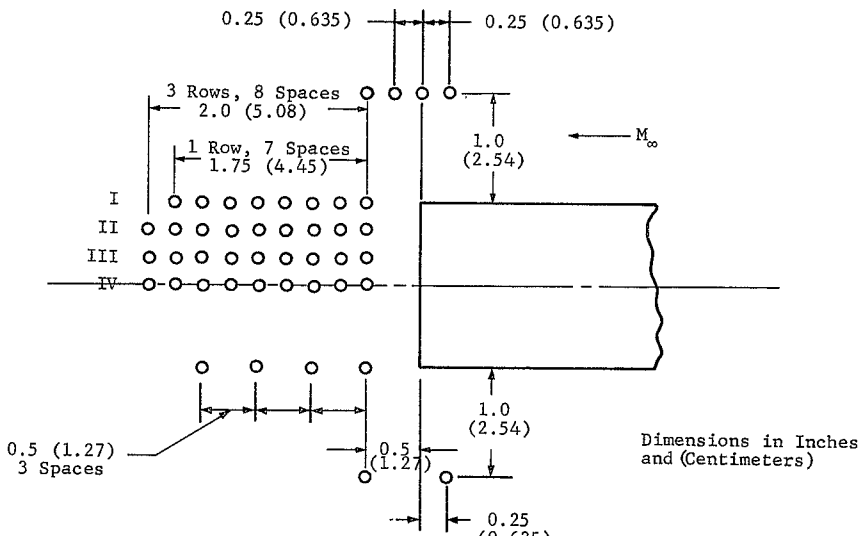

Fig. 17. LOCATION OF STATIC TAPS ON WIND TUNNEL WALL. 45 Holes, Diameter = 0.031 in. (0.0645 cm).

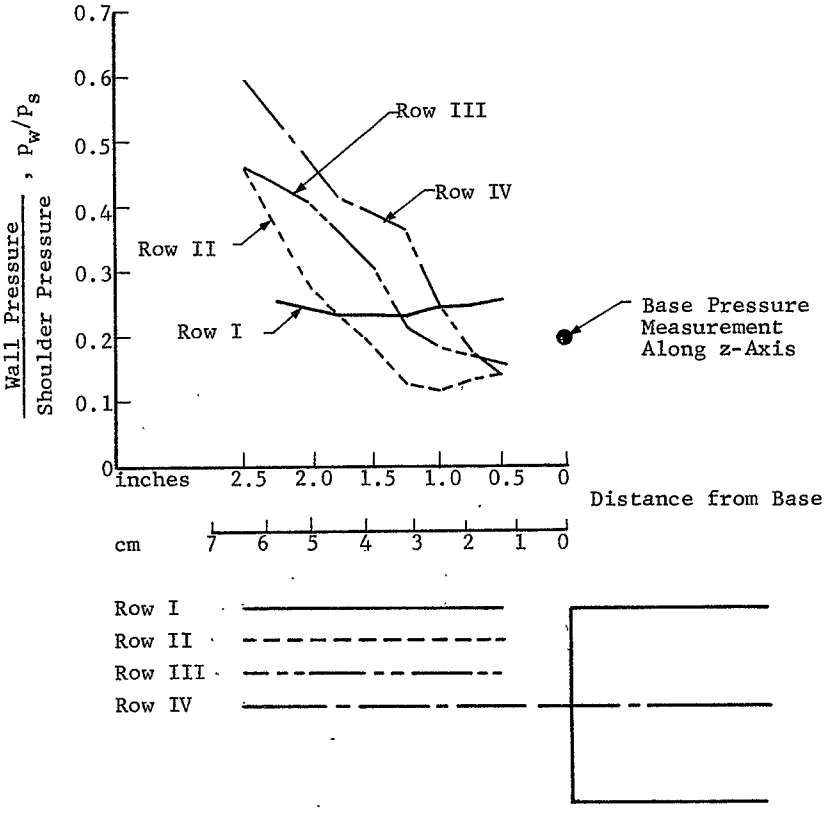

Fig. 18(a). TUNNEL WALL TO MODEL SHOULDER PRESSURE RATIO VERSUS DISTANCE FROM BASE AT $Re_\infty = 6.5 \times 10^6$

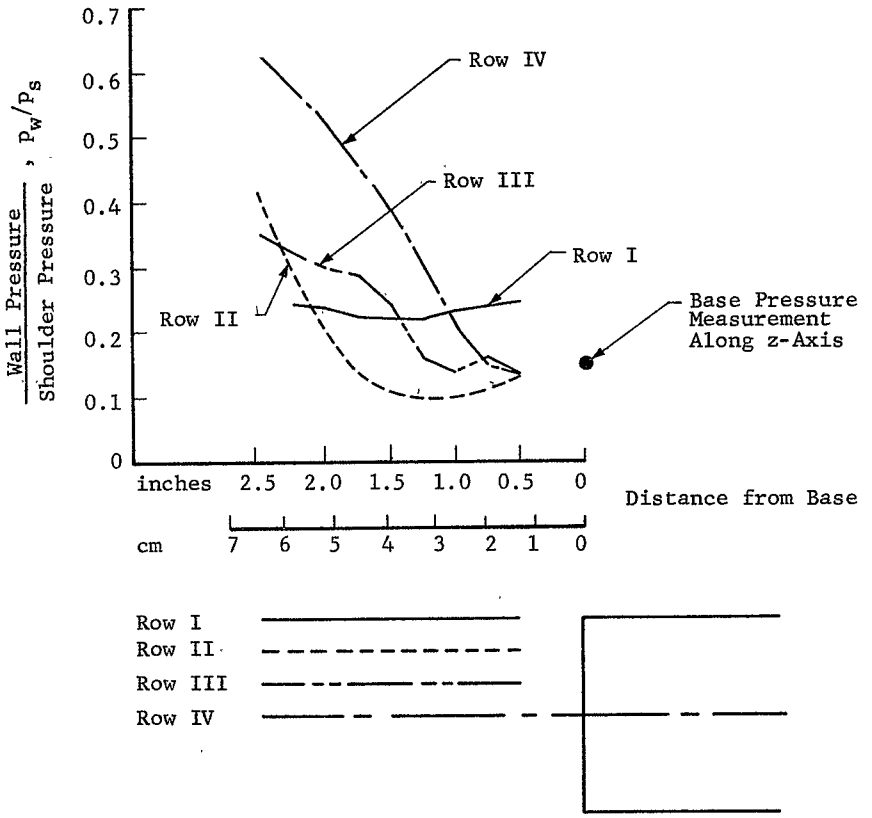

Fig. 18(b). TUNNEL WALL TO MODEL SHOULDER PRESSURE RATIO VERSUS DISTANCE FROM BASE AT $Re_\infty = 22.6 \times 10^6$

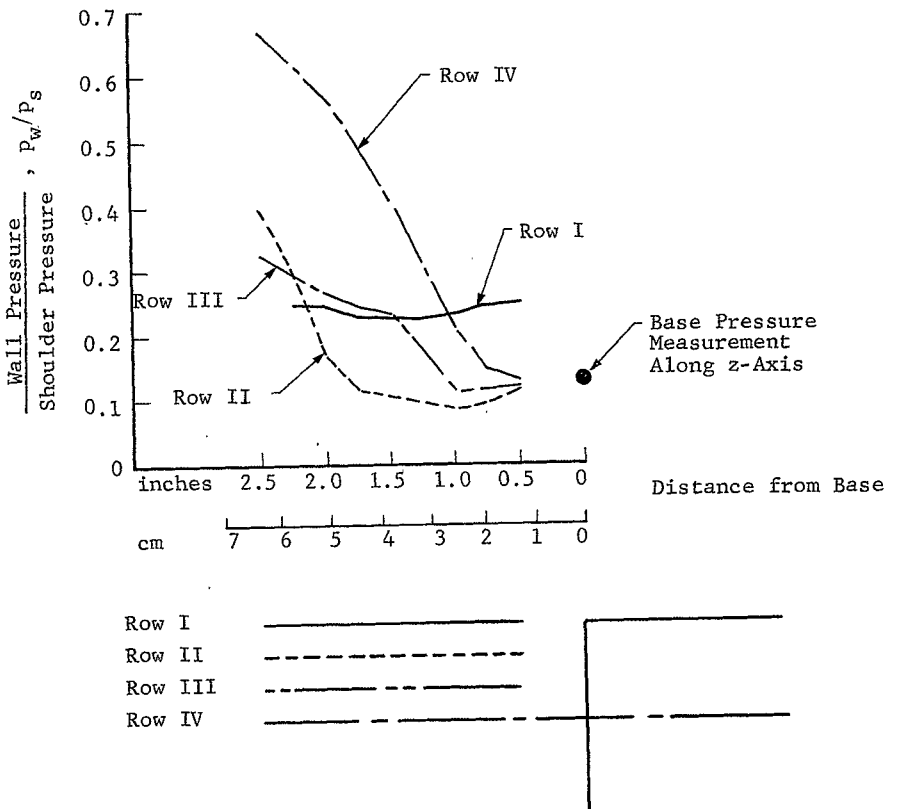

Fig. 18(c). TUNNEL WALL TO MODEL SHOULDER PRESSURE RATIO VERSUS DISTANCE FROM BASE AT $Re_\infty = 41 \times 10^6$

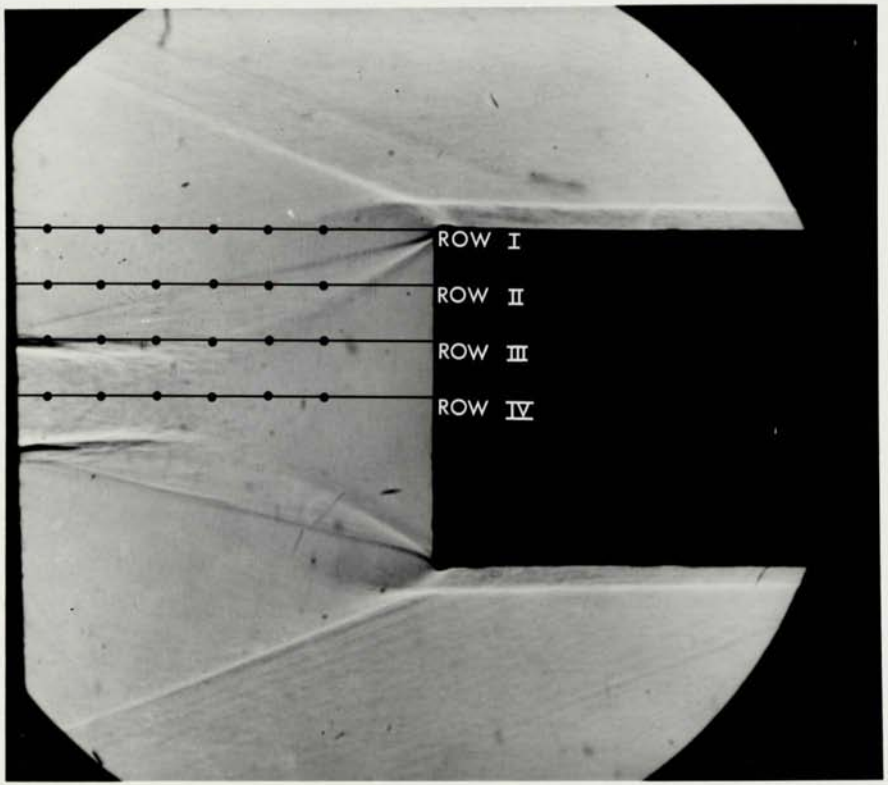

Fig. 19(a). SHADOWGRAPH OF BASE RECIRCULATION REGION AT $M_\infty = 2.97$ AND $Re_\infty = 6.5 \times 10^6$. Horizontal lines represent rows of tunnel wall static taps.

NOT REPRODUCIBLE

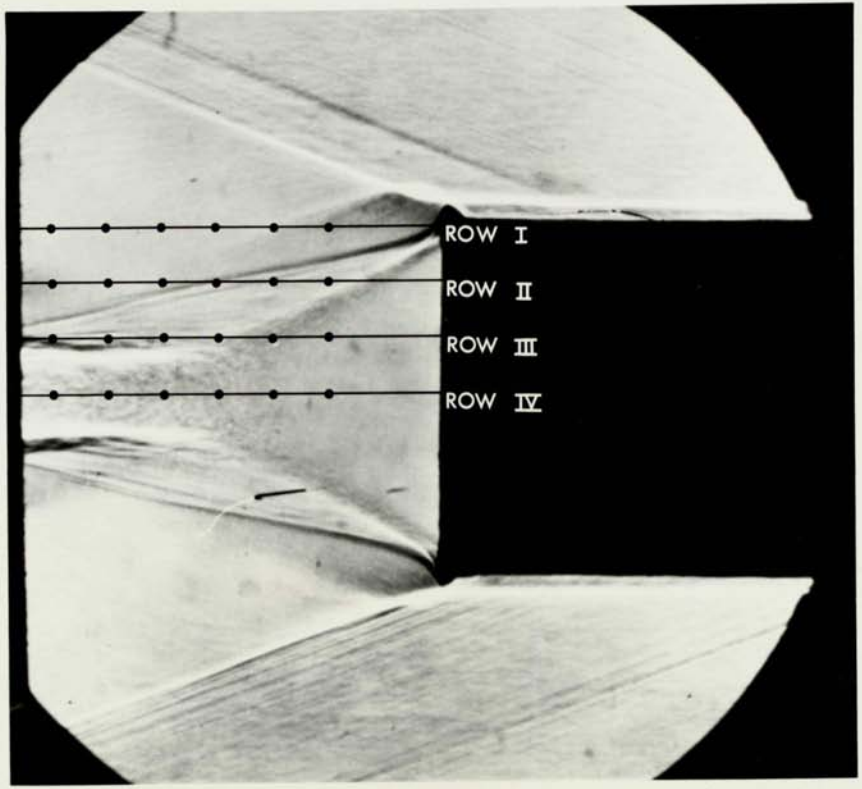

NOT REPRODUCIBLE

Fig. 19(b). SHADOWGRAPH OF BASE RECIRCULATION REGION AT $M_\infty = 2.97$ AND $Re_\infty = 22.6 \times 10^6$. Horizontal lines represent rows of tunnel wall static taps.

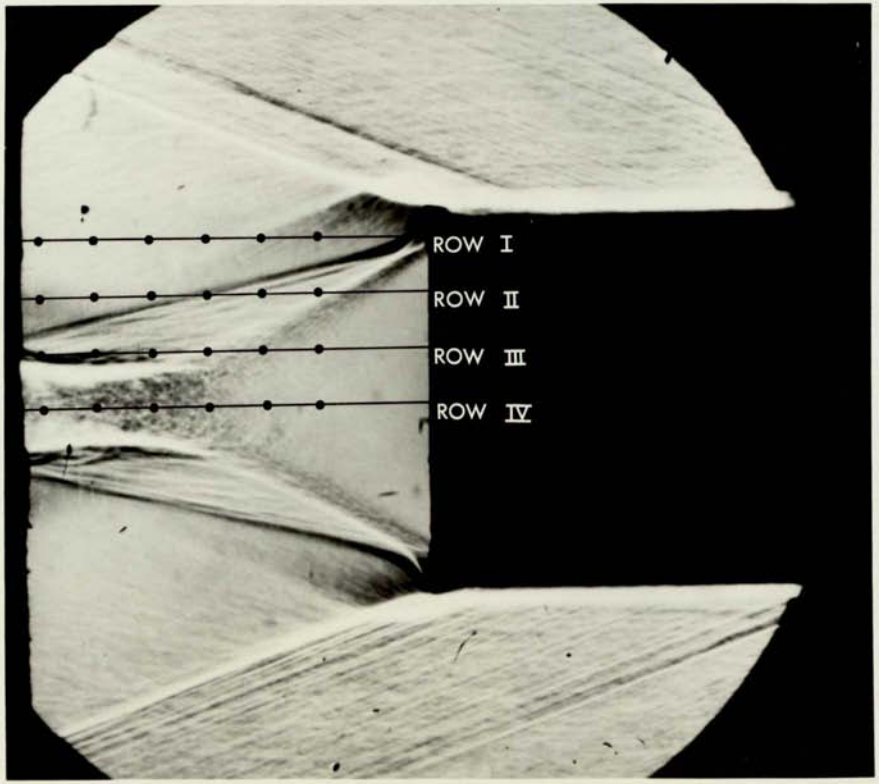

Fig. 19(c). SHADOWGRAPH OF BASE RECIRCULATION REGION AT $M_\infty = 2.97$ AND $Re_\infty = 41.0 \times 10^6$. Horizontal lines represent rows of tunnel wall static taps.

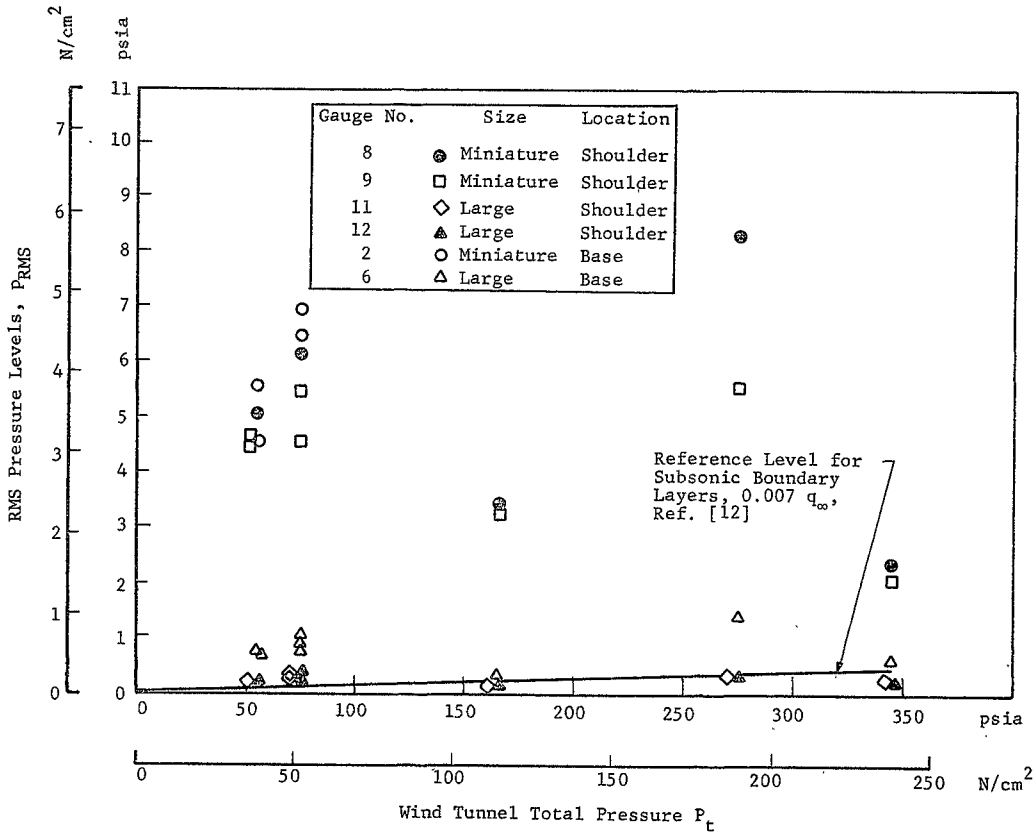

Fig. 20. RMS PRESSURE LEVELS FROM MINIATURE AND LARGE PZT-5H TRANSDUCERS. Calibration: 0.001 v/psi (0.00145 v/N/cm^2 for Miniature Gauges, D = 0.025 in. (0.0635 cm); 0.030 v/psi (0.0435 v/N/cm^2) for Large Gauges, D = 0.062 in. (0.1575 cm).

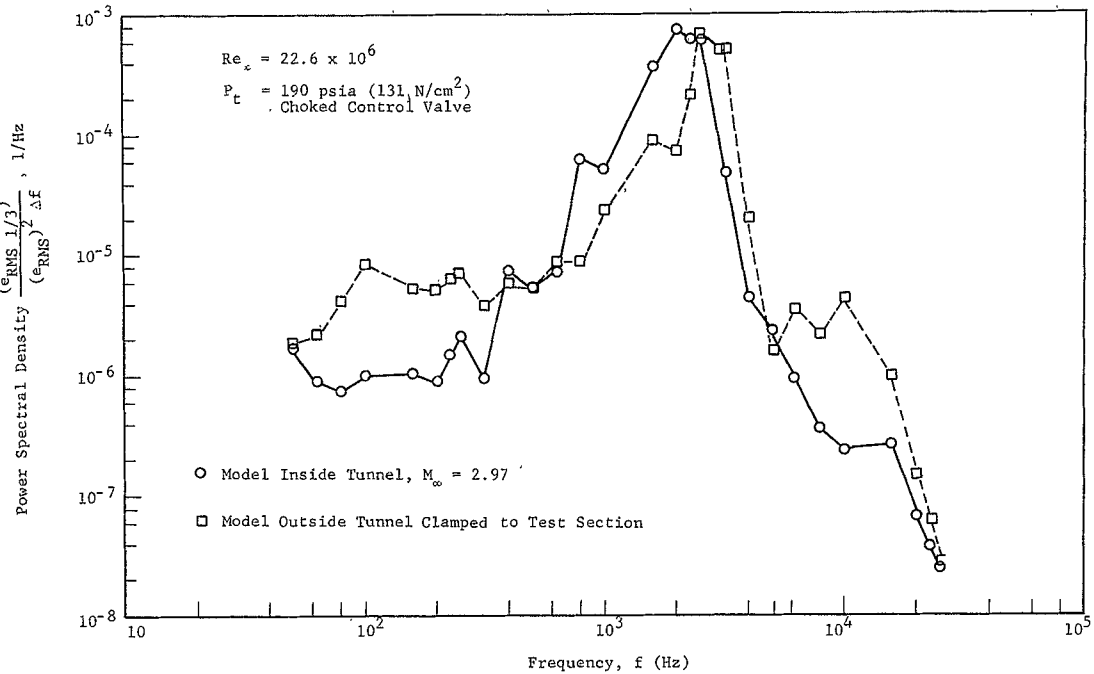

Fig. 21. POWER SPECTRAL DENSITY FOR PZT GAUGE NO. 3 LOCATED NEAR BASE CENTER.

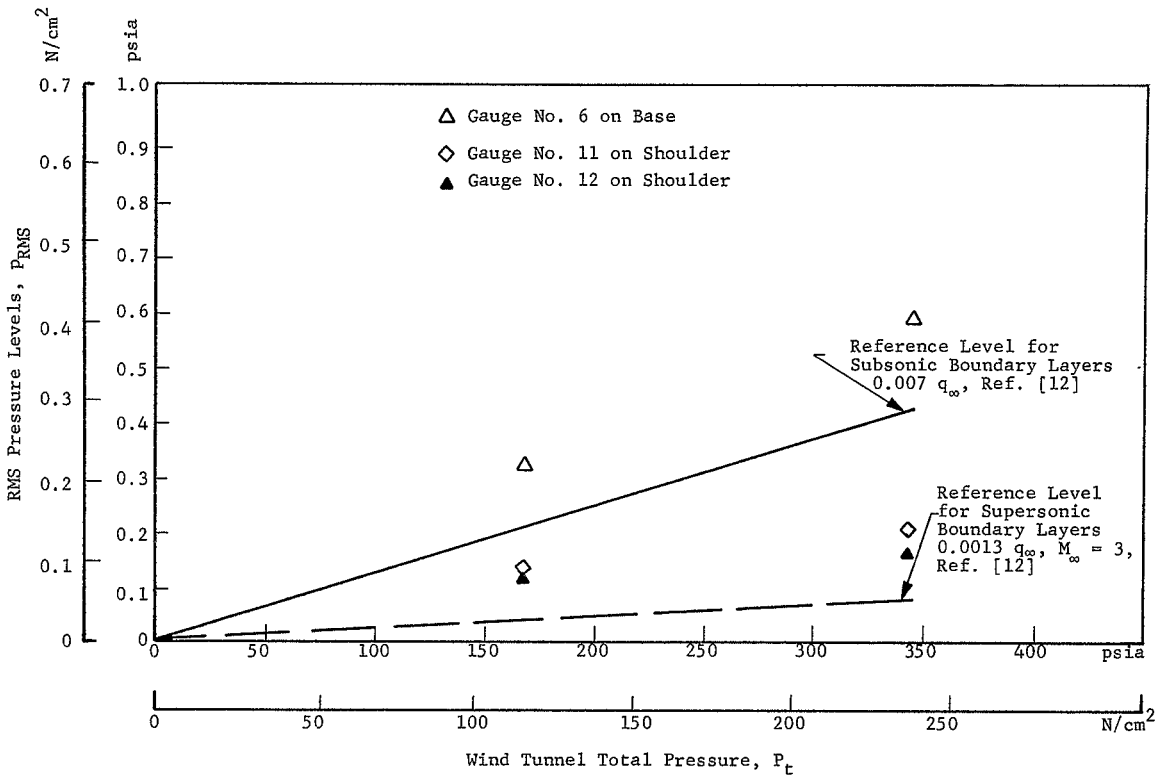

Fig. 22. FLUCTUATING PRESSURE LEVELS FOR LARGE GAUGES AT UNCHOKED CONTROL VALVE CONDITIONS.

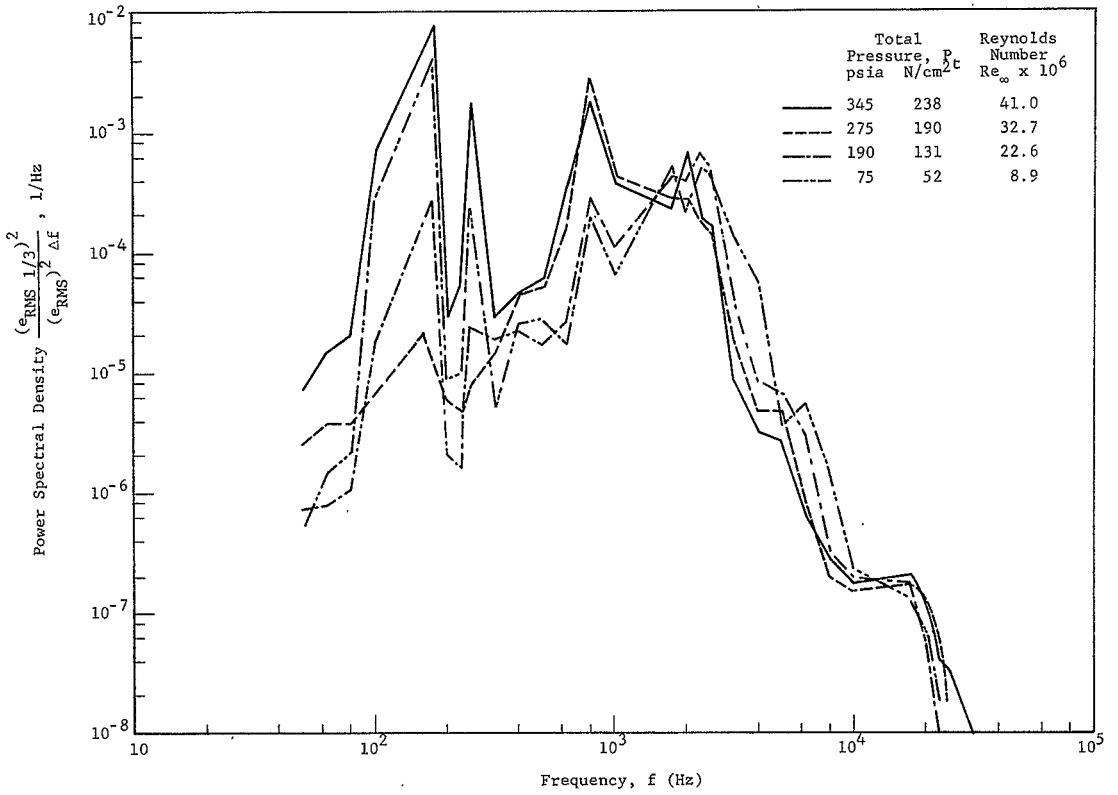

Fig. 23. POWER SPECTRAL DENSITY FOR LARGE TRANSDUCER GAUGE NO. 6 ON BASE PLATE.

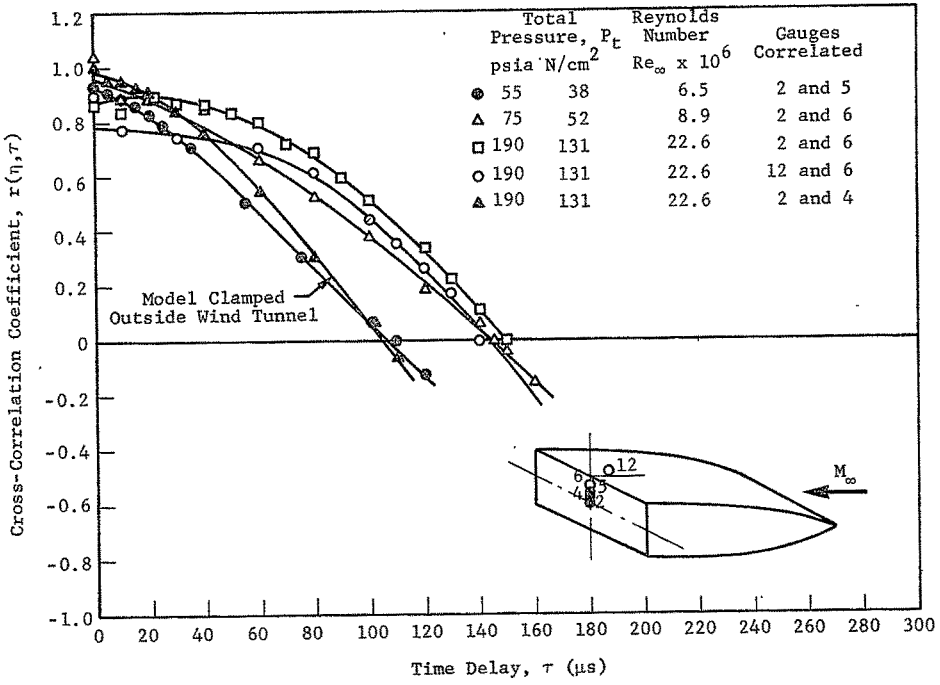

Fig. 24. CROSS-CORRELATION OF SEVERAL PRESSURE TRANSDUCERS FOR CHOKED CONTROL VALVE.

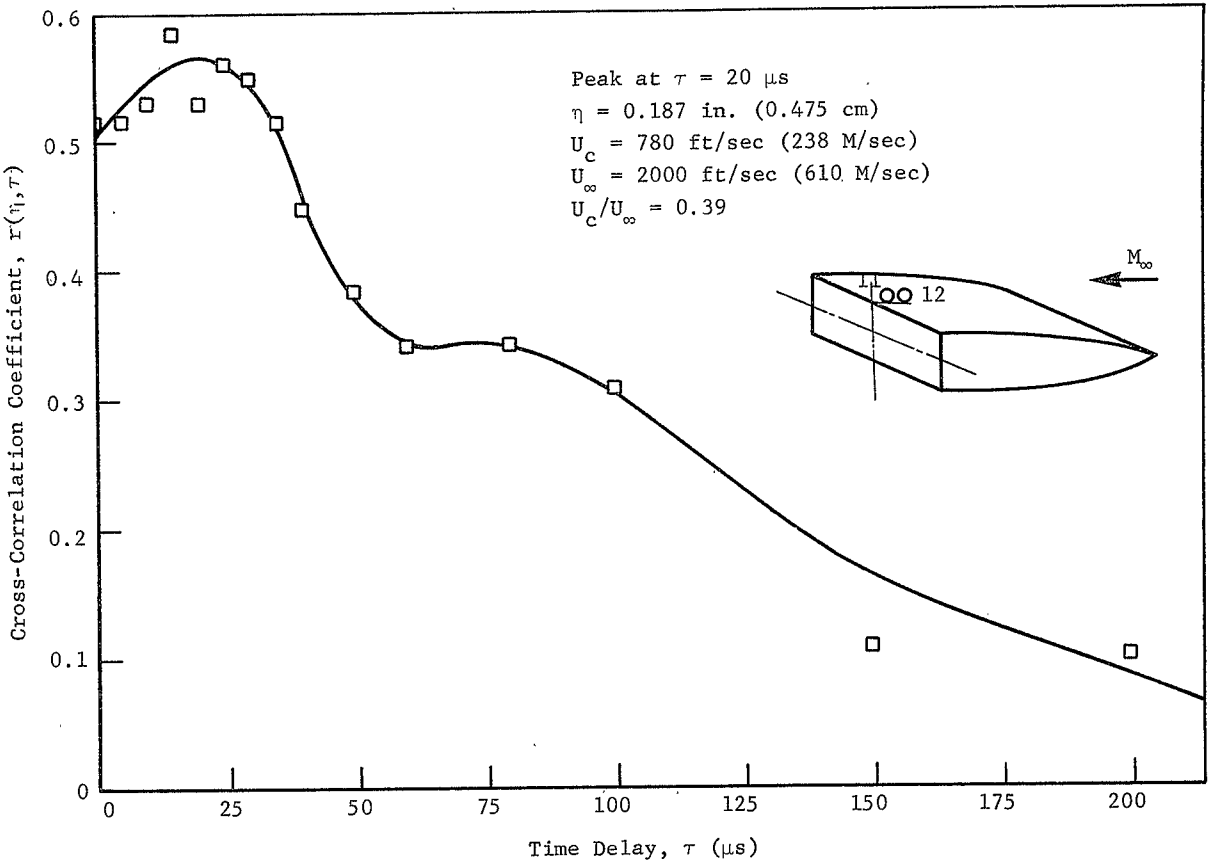

Fig. 25(a). CROSS-CORRELATION COEFFICIENT FOR PRESSURE TRANSDUCER GAUGES 12 AND 11, P_t = 345 psia (238 N/cm^2), $Re_\infty = 41 \times 10^6$ UNCHOKED CONTROL VALVE

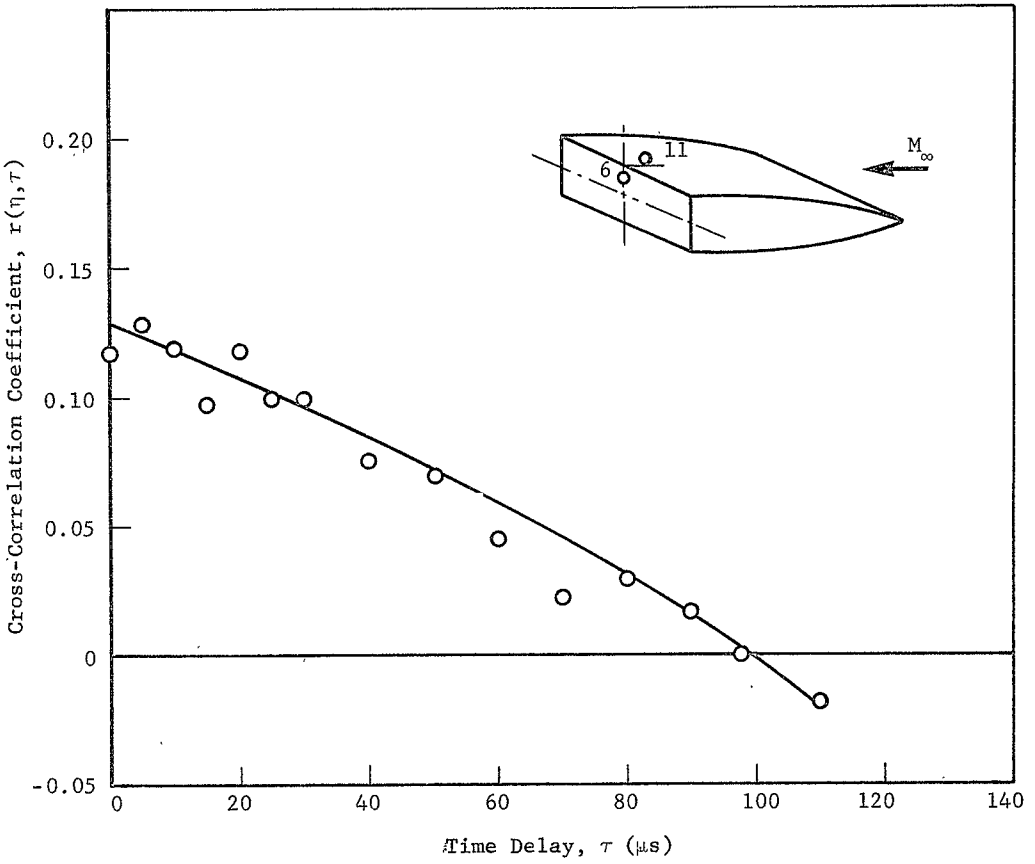

Fig. 25(b). CROSS-CORRELATION COEFFICIENT FOR PRESSURE TRANSDUCER GAUGES 11 AND 6, P_t = 345 psia (238 N/cm^2), Re_∞ = 41 x 10^6 UNCHOKED CONTROL VALVE

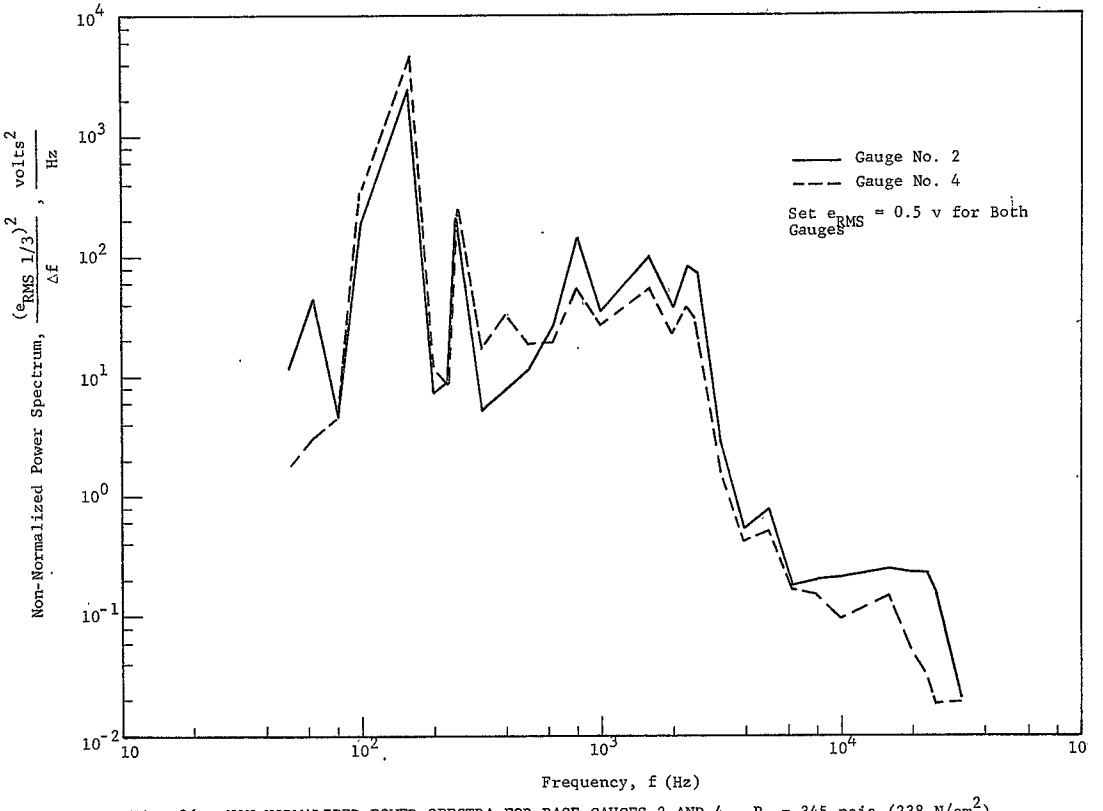

Fig. 26. NON-NORMALIZED POWER SPECTRA FOR BASE GAUGES 2 AND 4. P_t = 345 psia (238 N/cm^2), $Re_\infty = 41 \times 10^6$, Unchoked Control Valve.

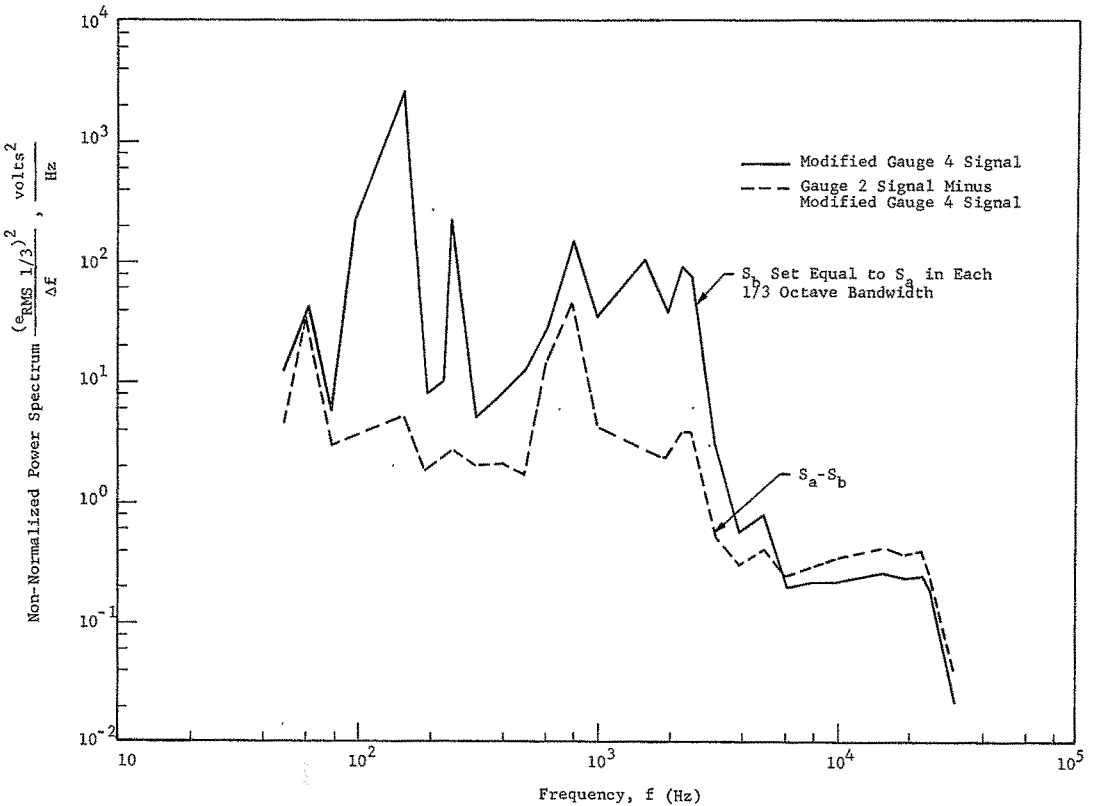

Fig. 27. NON-NORMALIZED POWER SPECTRA WITH GAUGE 2 SIGNAL, S_a, EQUAL TO MODIFIED GAUGE 4 SIGNAL, S_b, AND DIFFERENCE SIGNAL S_a-S_b. P_t = 345 psia (238 N/cm^2), Re_∞ = 41 x 10^6, Unchoked Control Valve.

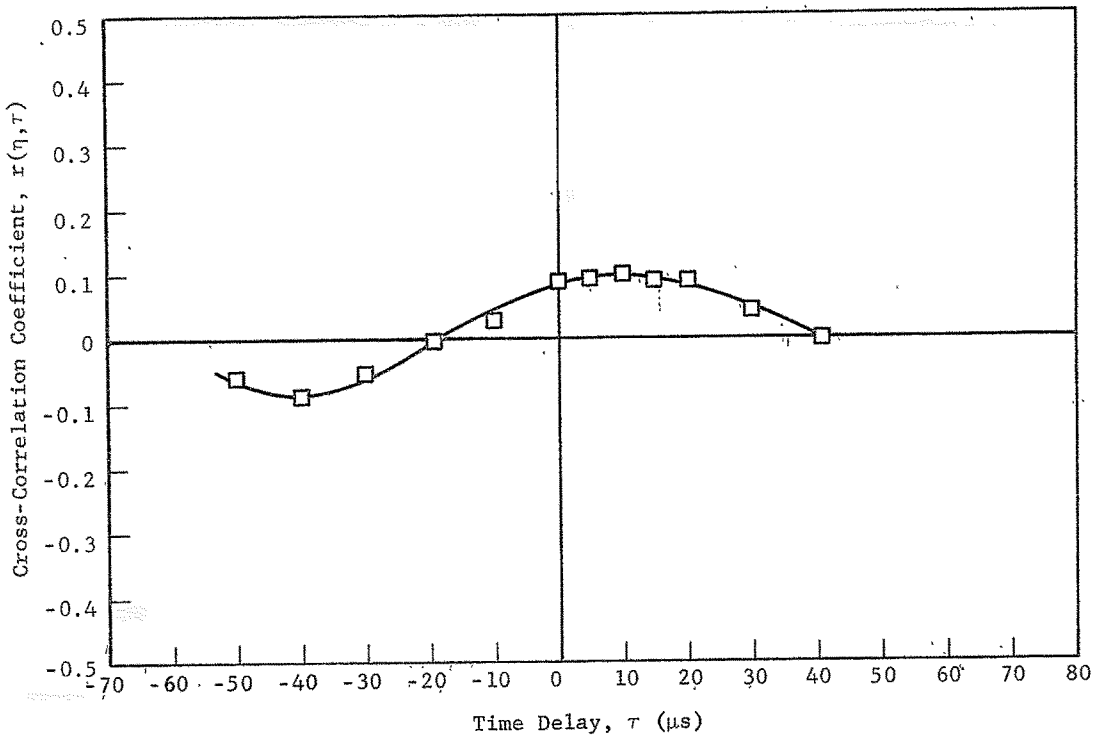

Fig. 28. CROSS-CORRELATION FOR PRESSURE TRANSDUCER GAUGES 2 AND 4 OVER 1/3 OCTAVE BANDWIDTH AT 10,000 Hz CENTER FREQUENCY P_t = 345 psia (238 N/cm^2), Re_∞ = 41 x 10^6 UNCHOKED CONTROL VALVE

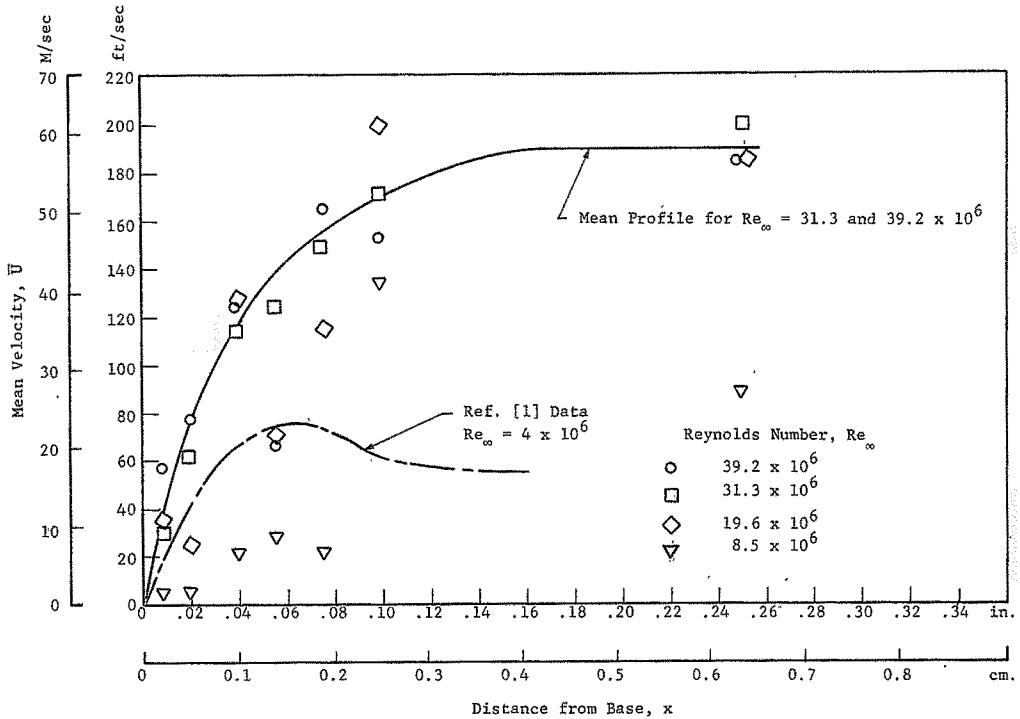

Fig. 29. BASE BOUNDARY LAYER PROFILE. Mean Velocity Versus Horizontal Distance from Base for Probe Position 2P for Several Reynolds Numbers, Base Plate at Room Temperature.

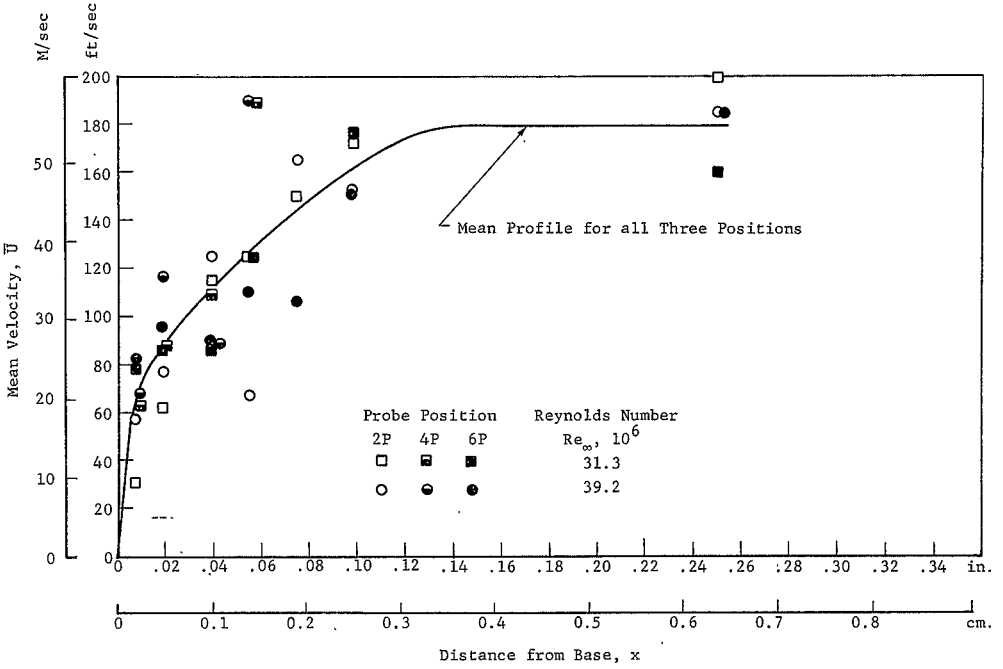

Fig. 30. BASE BOUNDARY LAYER PROFILE. Mean Velocity Versus Horizontal Distance from Base for Three Probe Positions and Two Reynolds Numbers, Base at Room Temperature.

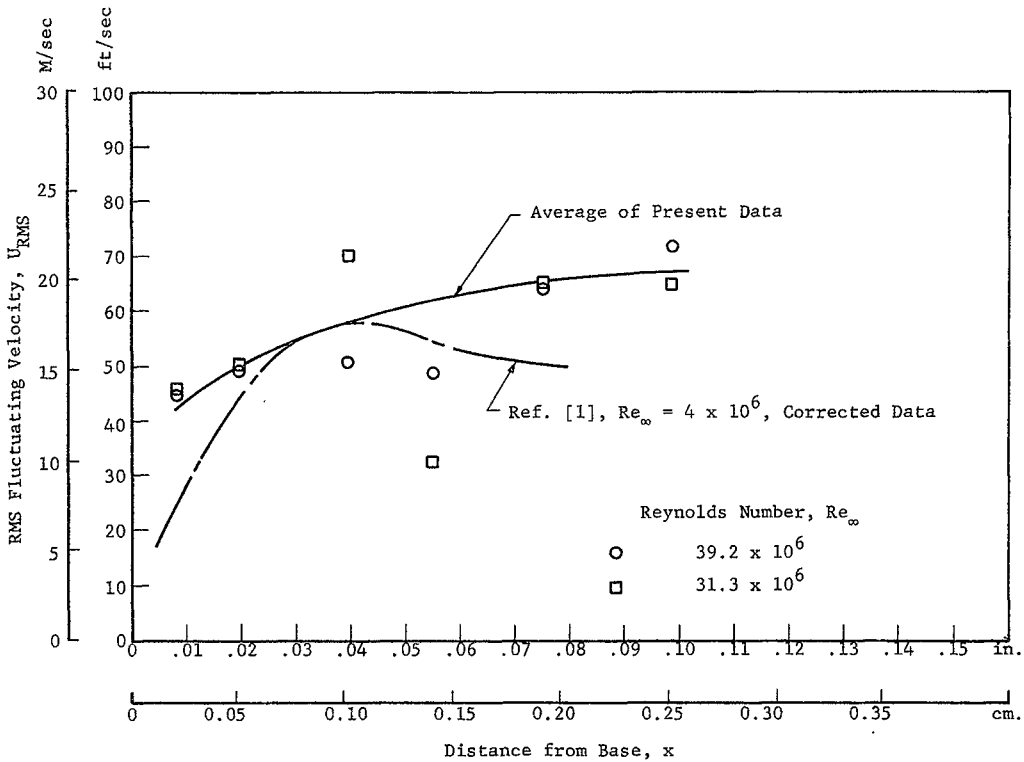

Fig. 31. RMS FLUCTUATING VELOCITY VERSUS DISTANCE FROM BASE AT HIGH REYNOLDS NUMBERS. Base at Room Temperature, Probe Position 2P.

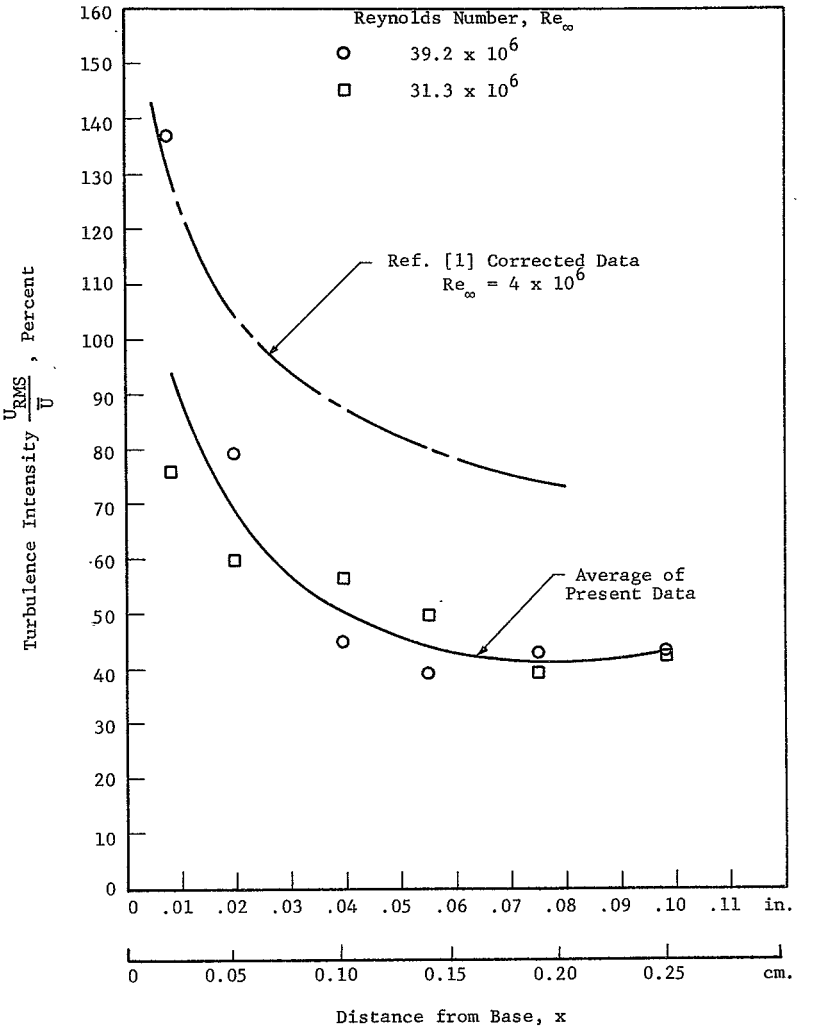

Fig. 32. TURBULENCE INTENSITY $U_{RMS}/\bar{U}$ VS DISTANCE FROM BASE FOR PROBE POSITION (2P). Base at Room Temperature.

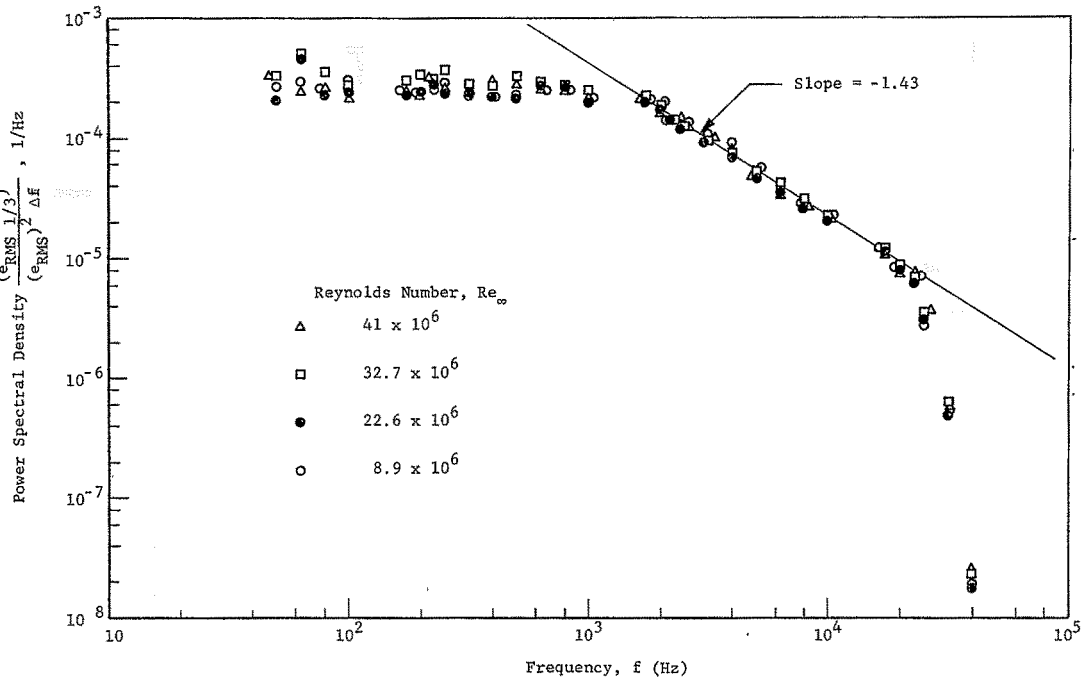

Fig. 33. POWER SPECTRAL DENSITY FOR HOT WIRE AT PROBE POSITION H1. Distance from Base = 0.028 in. (0.071 cm), Base at Room Temperature, Varying Reynolds Number.

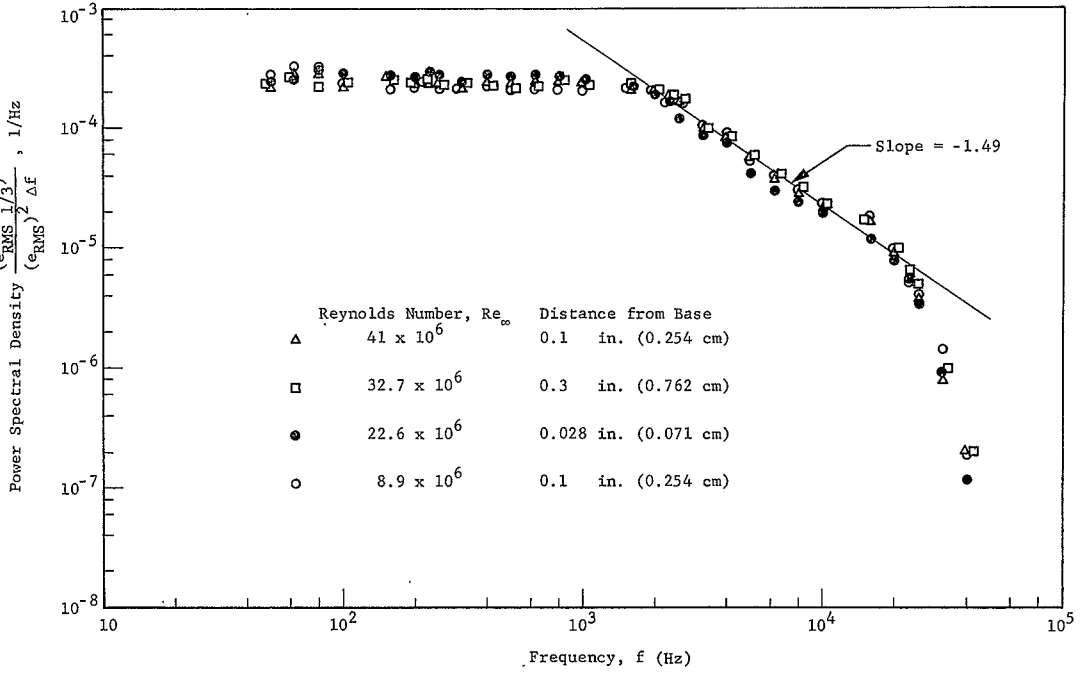

Fig. 34. POWER SPECTRAL DENSITY FOR HOT WIRE AT PROBE POSITION H2. Base at Room Temperature, Distance from Base Varying.

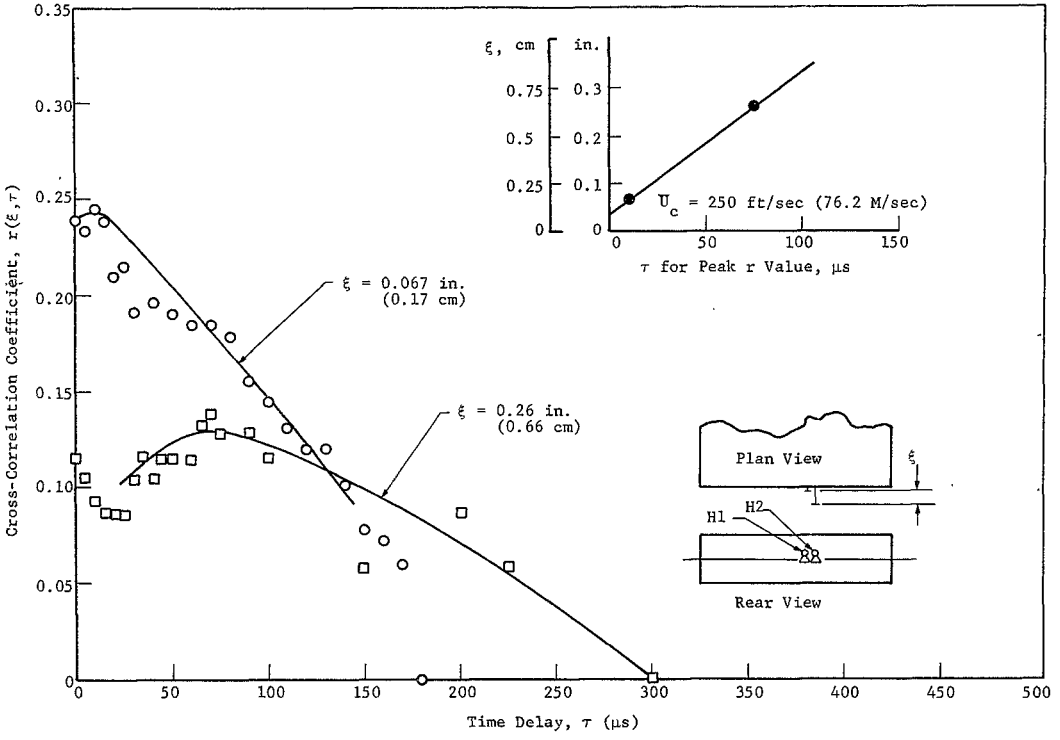

Fig. 35(a). CROSS-CORRELATION OF HOT WIRES H1 AND H2 INCLUDING COMPUTATION OF CONVECTION VELOCITY. P_t = 75 psia (52 N/cm^2), $Re_\infty = 8.9 \times 10^6$.

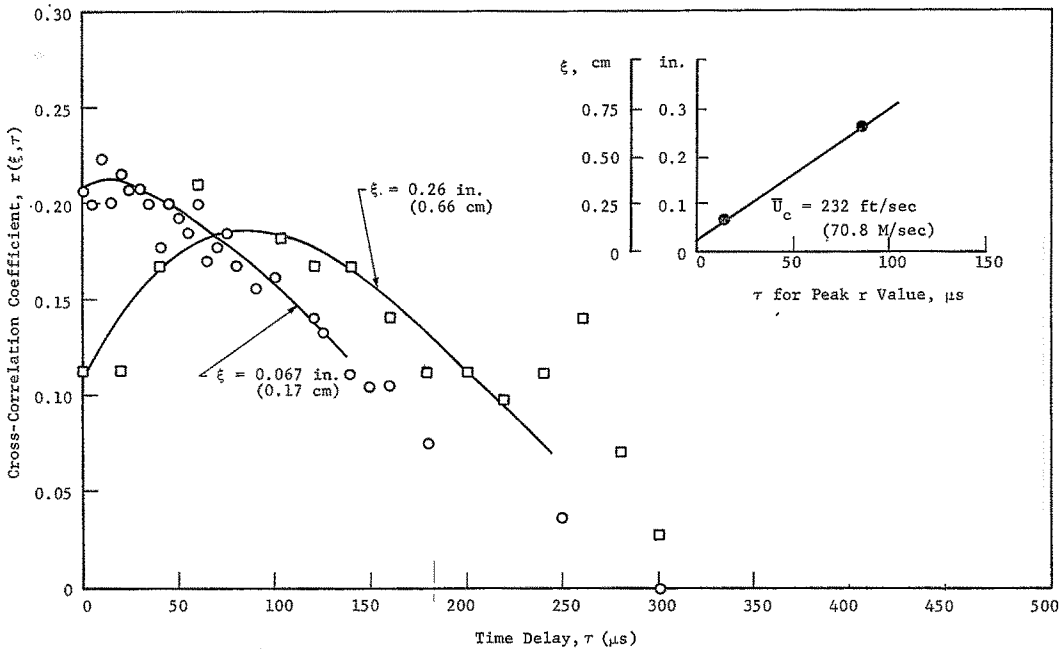

Fig. 35(b). CROSS-CORRELATION OF HOT WIRES H1 AND H2 INCLUDING COMPUTATION OF CONVECTION VELOCITY. P_t = 190 psia (131 N/cm^2), $Re_\infty = 22.6 \times 10^6$.

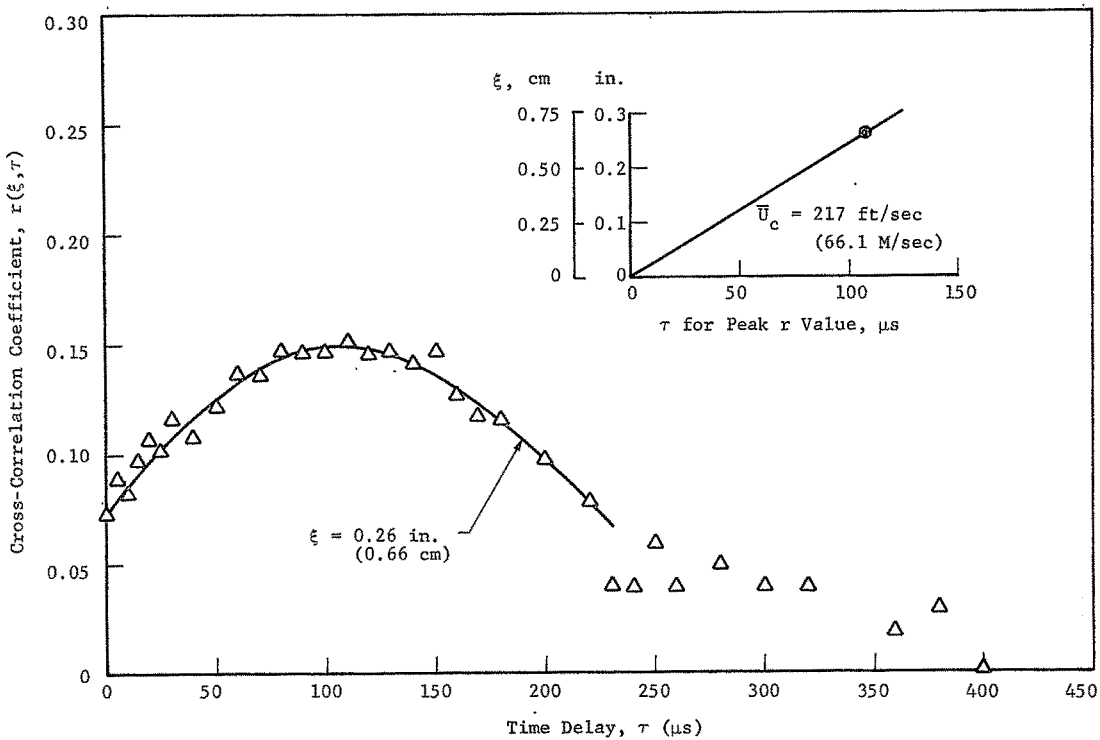

Fig. 35(c). CROSS-CORRELATION OF HOT WIRES H1 AND H2 INCLUDING COMPUTATION OF CONVECTION VELOCITY. P_r = 275 psia (190 N/cm^2), Re_∞ = 32.7 x 10^6.

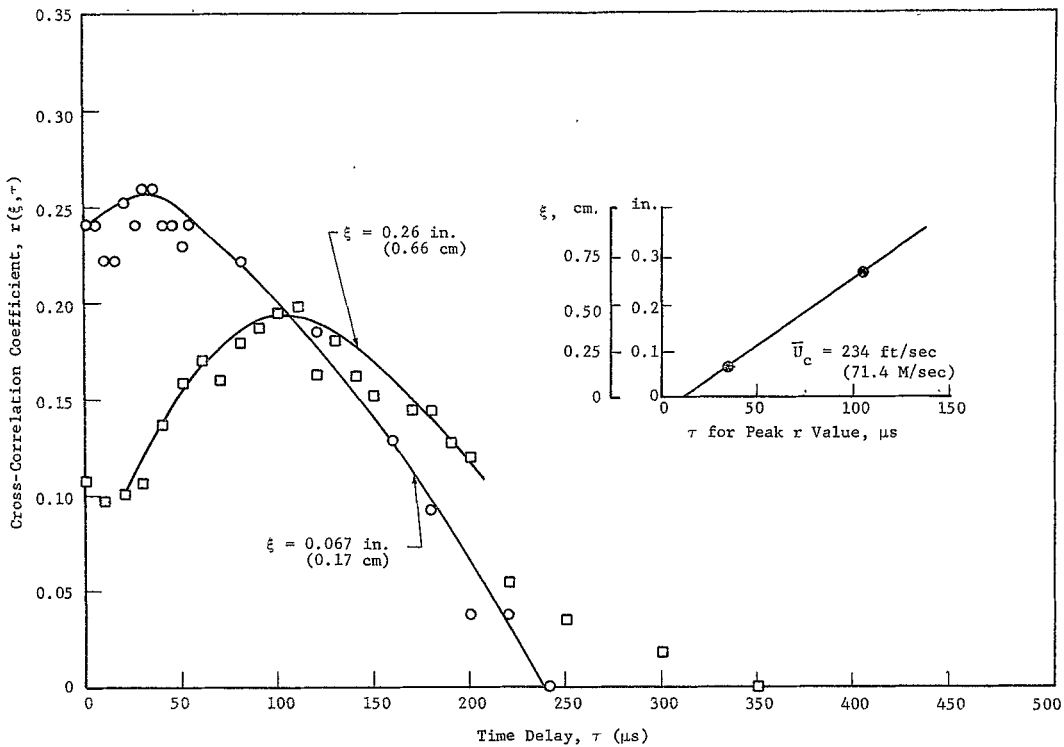

Fig. 35(d). CROSS-CORRELATION OF HOT WIRES H1 AND H2 INCLUDING COMPUTATION OF CONVECTION VELOCITY. P_t = 345 psia (238 N/cm^2), $Re_\infty = 41 \times 10^6$.

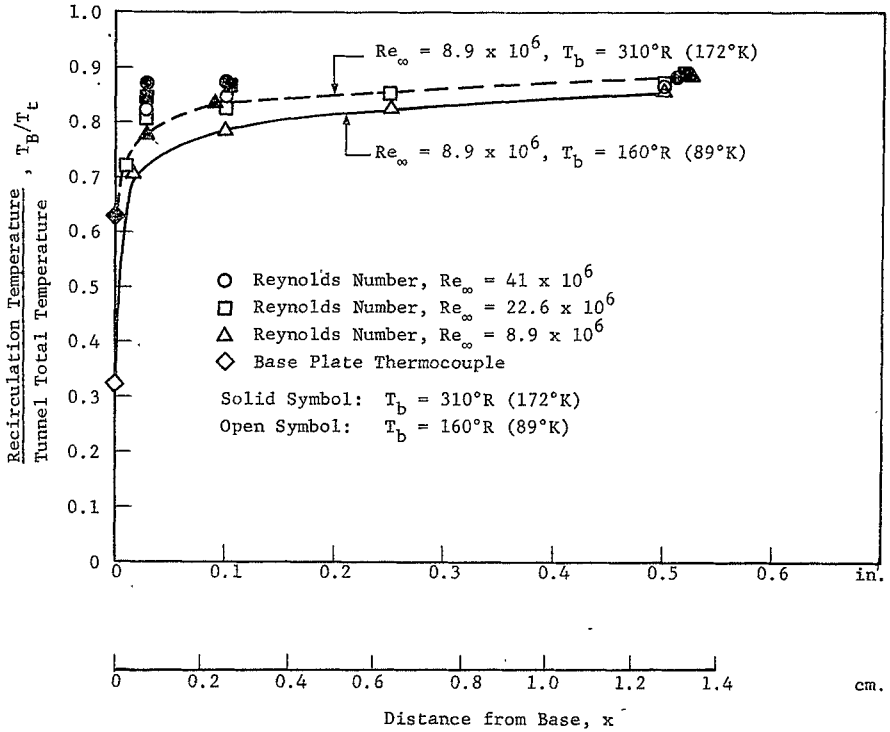

Fig. 36. RECIRCULATION TEMPERATURE TO TOTAL TEMPERATURE RATIO VS DISTANCE FROM BASE FOR THERMOCOUPLE PROBE TC3, POSITION 6P

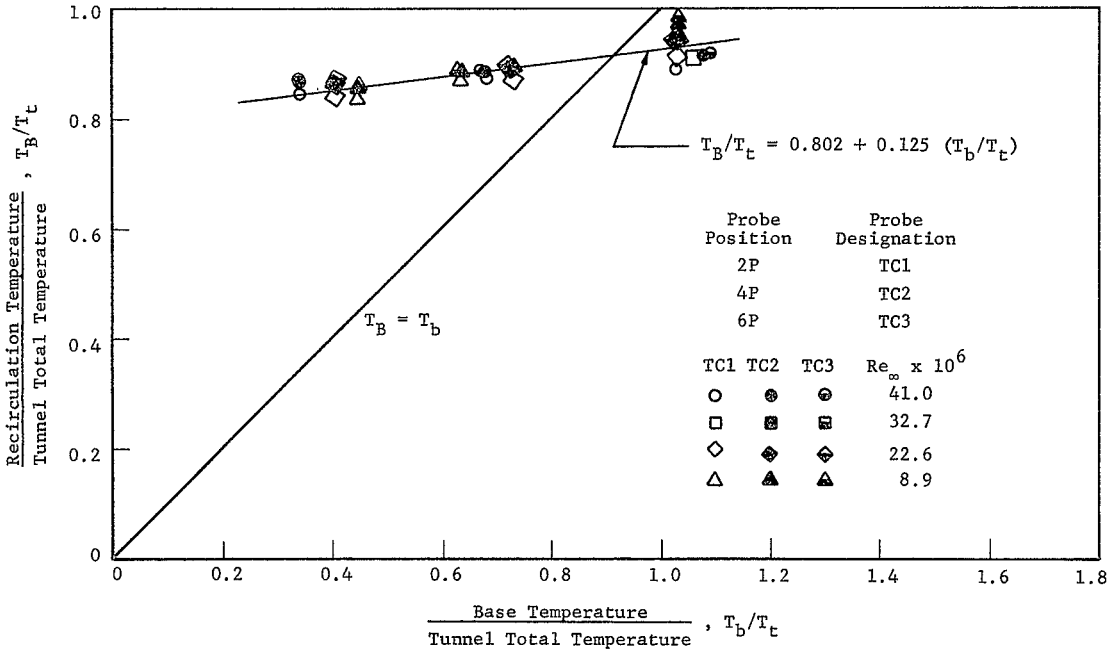

Fig. 37. RECIRCULATION TEMPERATURE RATIO VERSUS BASE TEMPERATURE RATIO FOR x = 0.5 in. (1.27 cm) AND ALL THERMOCOUPLE PROBES

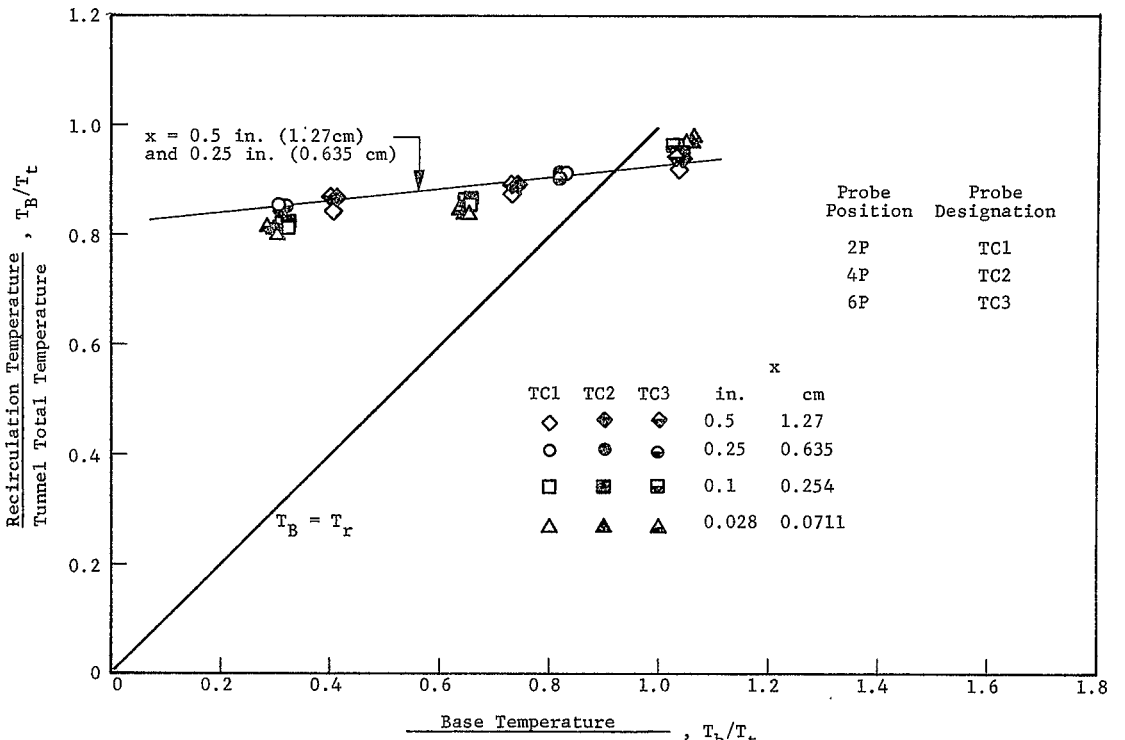

Fig. 38. RECIRCULATION TEMPERATURE RATIO VERSUS BASE TEMPERATURE RATIO FOR $Re_\infty = 22.6 \times 10^6$ AND ALL THERMOCOUPLE PROBES

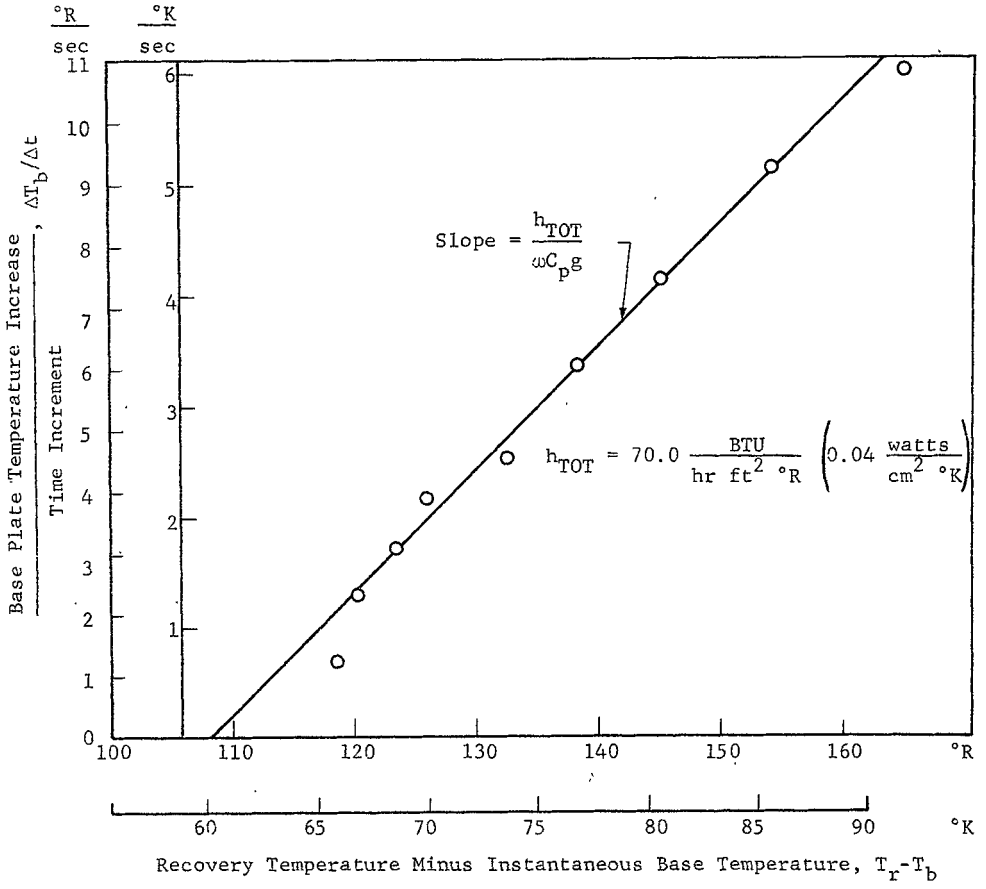

Fig. 39. COMPUTATION OF HEAT TRANSFER COEFFICIENT FROM TRANSIENT BASE PLATE TEMPERATURE RISE; For Run 68, $Re_\infty = 39.2 \times 10^6$, Thermocouple TC 11, and Initial Base Temperature = 300°R (167°K)

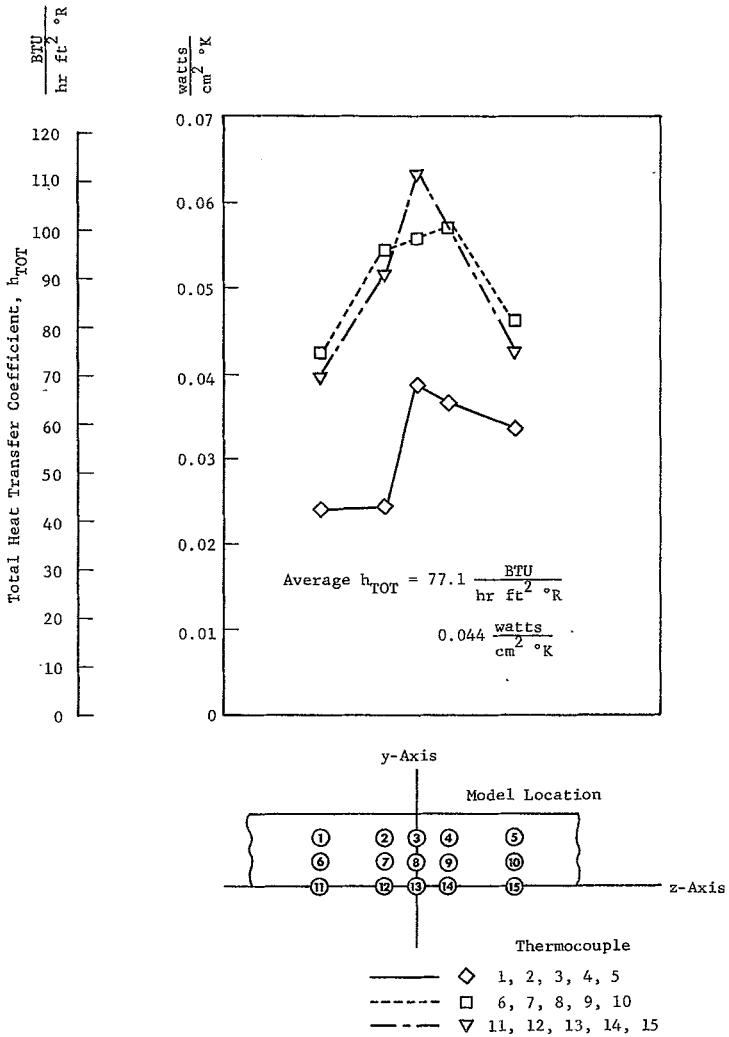

Fig. 40. DISTRIBUTION OF TOTAL HEAT TRANSFER COEFFICIENT OVER BASE PLATE. $Re_\infty = 39.2 \times 10^6$, Initial Base Temperature $T_b = 300°R$ (167°K)

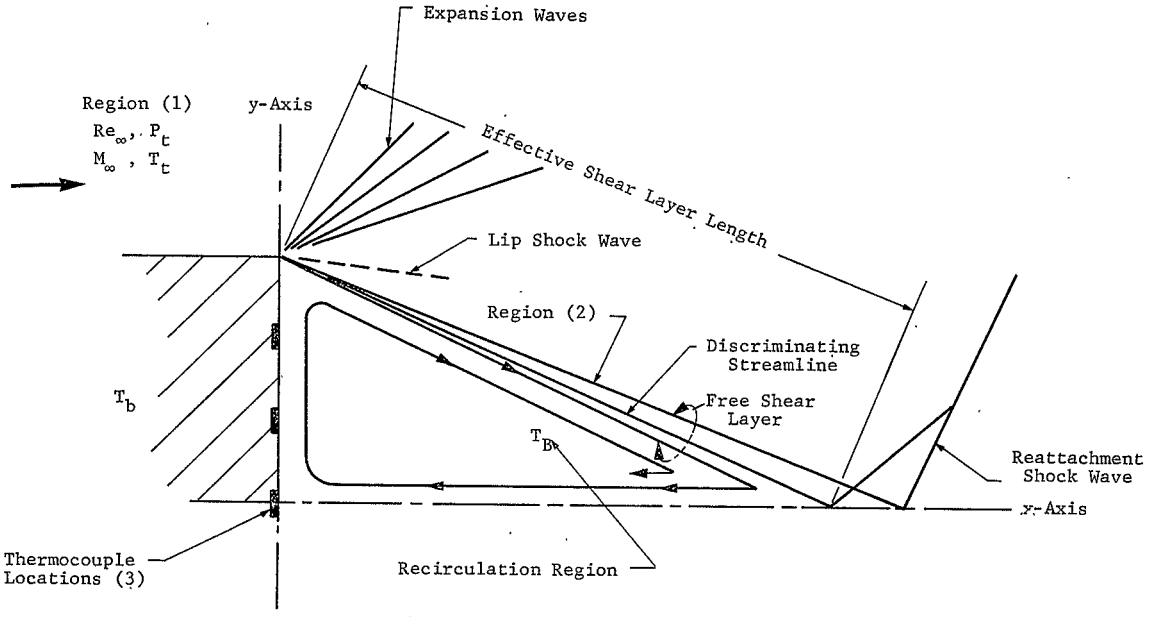

Fig. 41. SCHEMATIC OF BASE FLOW RECIRCULATION REGION

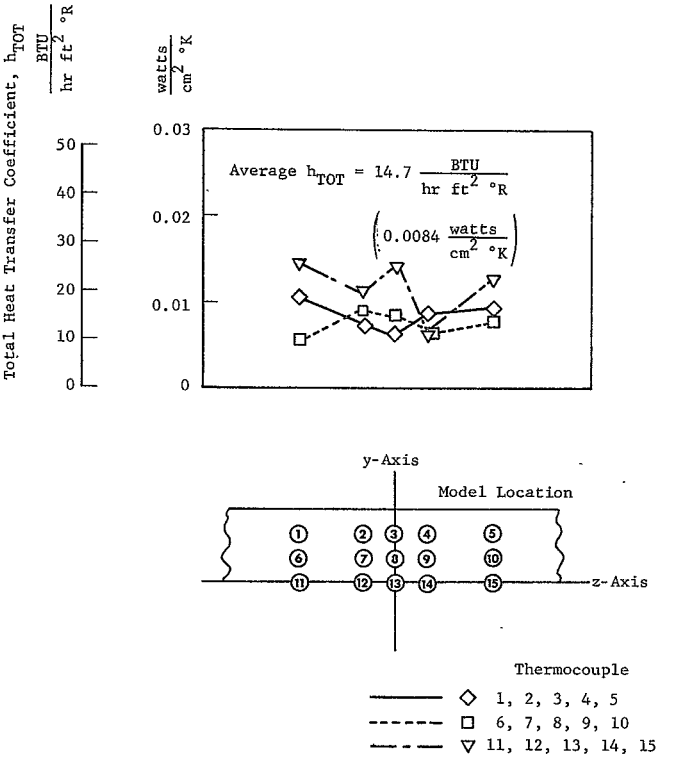

Fig. 42. DISTRIBUTION OF TOTAL HEAT TRANSFER COEFFICIENT OVER BASE PLATE. $Re_\infty = 6.8 \times 10^6$, Initial Base Temperature T_b = 310°R (172°K)

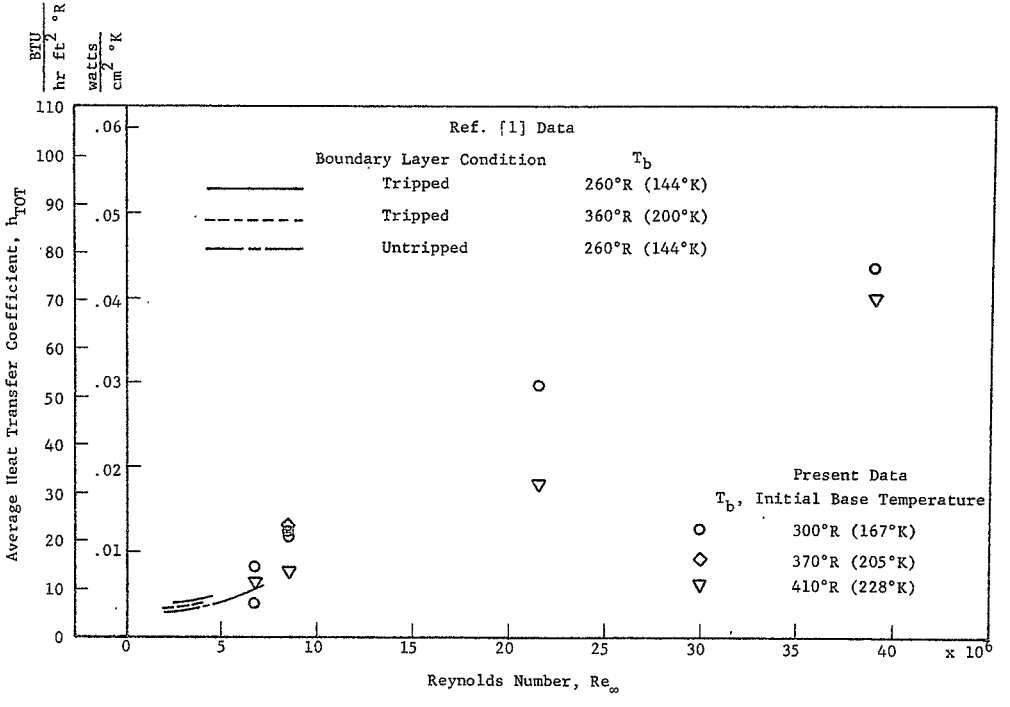

Fig. 43. AVERAGE HEAT TRANSFER COEFFICIENT VERSUS REYNOLDS NUMBER

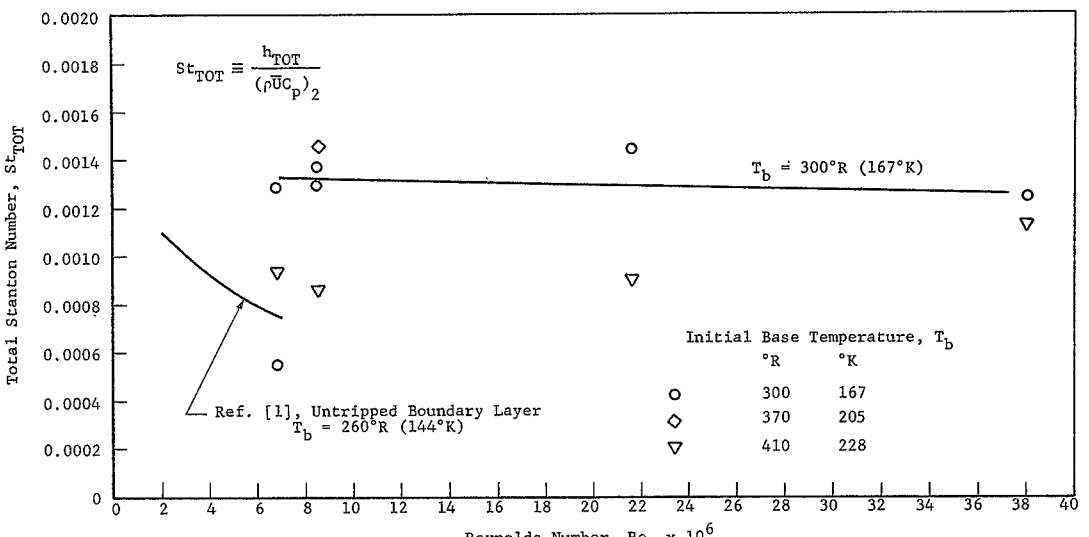

Fig. 44. TOTAL STANTON NUMBER VERSUS REYNOLDS NUMBER FOR DIFFERENT BASE TEMPERATURES

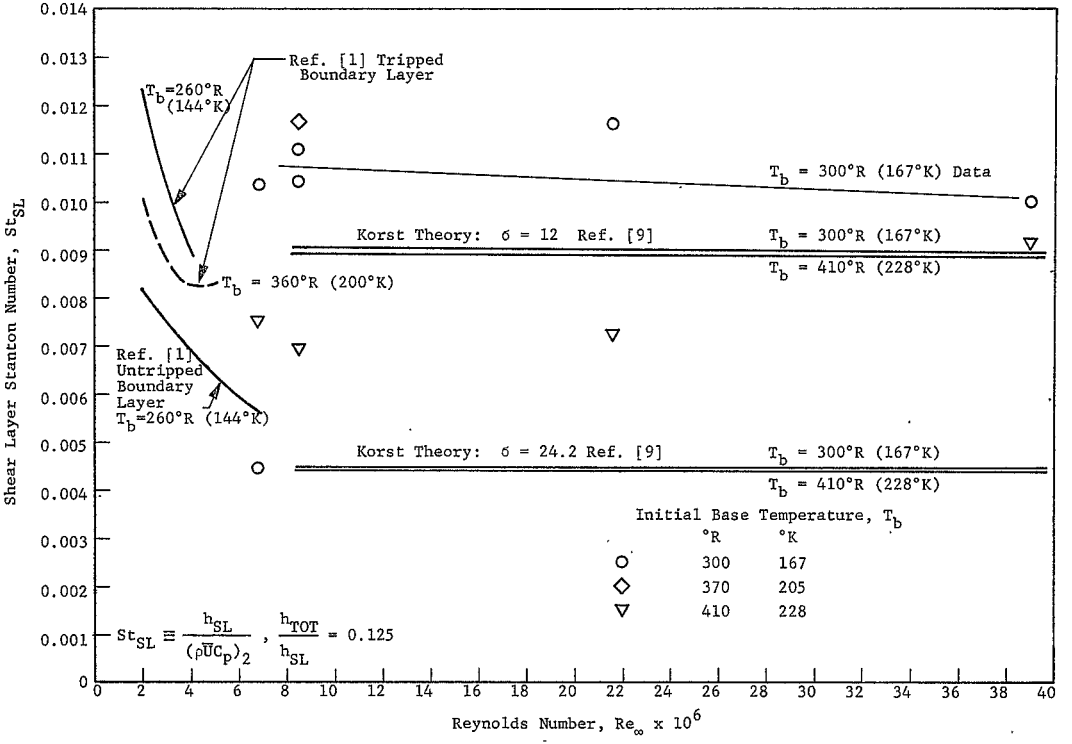

Fig. 45. SHEAR LAYER STANTON NUMBER VERSUS REYNOLDS NUMBER FOR DIFFERENT BASE TEMPERATURES

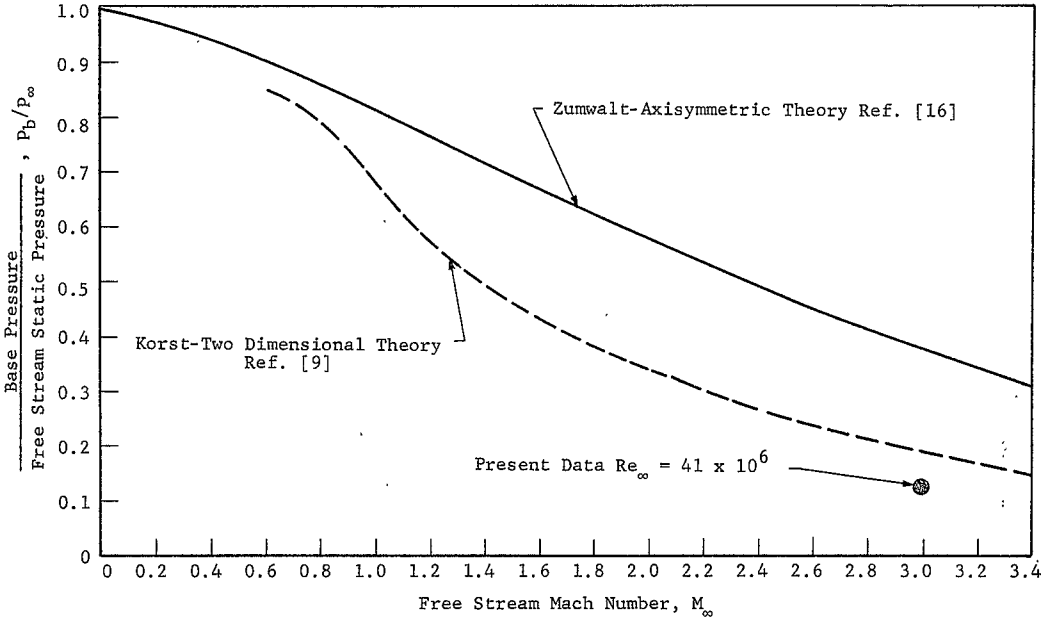

Fig. 46. BASE PRESSURE RATIO COMPARISON FOR TWO-DIMENSIONAL AND AXISYMMETRIC THEORIES

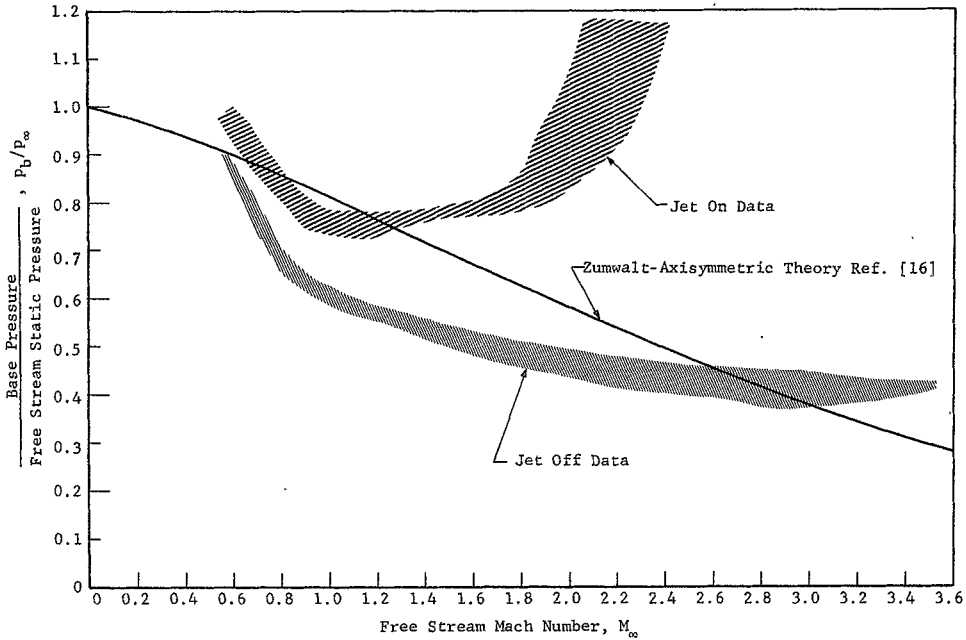

Fig. 47. BASE PRESSURE RATIO VERSUS MACH NUMBER FOR SATURN SIC BOOSTER MODEL, from NASA TN D-3612 [Ref. 17]